



Australia's National
Science Agency

Topic 2 – Analytical methods for determination of stable operation of IBRs in a future power system

2023/24 CSIRO GPST Research

Commonwealth Scientific and Industrial Research
Organization

Sushrut Thakar, Stavros Konstantinopoulos, Vishal Verma,
Deepak Ramasubramanian, Mobolaji Bello (EPRI), Jingzhe
Xu, Jaleel Mesbah, Weihua Zhou, Behrooz Bahrani (Monash
University)
30 April, 2024



MONASH
University

Citation

S. Thakar, S. Konstantinopoulos, V. Verma, D. Ramasubramanian, M. Bello, J. Xu, J. Mesbah, W. Zhou, and B. Bahrani (2024) Topic 2 – Analytical methods for determination of stable operation of IBRs in a future power system. CSIRO, Australia. Copyright

© Commonwealth Scientific and Industrial Research Organisation 2024. To the extent permitted by law, all rights are reserved and no part of this publication covered by copyright may be reproduced or copied in any form or by any means except with the written permission of CSIRO.

Important disclaimer

CSIRO advises that the information contained in this publication comprises general statements based on scientific research. The reader is advised and needs to be aware that such information may be incomplete or unable to be used in any specific situation. No reliance or actions must therefore be made on that information without seeking prior expert professional, scientific and technical advice. To the extent permitted by law, CSIRO (including its employees and consultants) excludes all liability to any person for any consequences, including but not limited to all losses, damages, costs, expenses and any other compensation, arising directly or indirectly from using this publication (in part or in whole) and any information or material contained in it.

CSIRO is committed to providing web accessible content wherever possible. If you are having difficulties with accessing this document please contact csiro.au/contact.

Contents

Acknowledgments.....	vii
Executive summary	viii
1 Introduction	1
1.1 Relation to Research Roadmap	2
1.2 Background work.....	4
1.3 Summary of work effort	7
2 Methodology followed in the project.....	8
3 Comparison of IBR admittance estimation methods	10
3.1 Method to compare performance	10
3.2 Comparison of the APM and DDPM	11
3.3 Investigation of the APM to inverter control structure and parameter sensitivities	14
4 Application of IBR admittance estimation method to a black box IBR model	18
4.1 Black box IBR model	18
4.2 Application of admittance estimation methods	20
5 A framework to analyse small signal stability of a network.....	27
5.1 Impact of EMT vs positive sequence admittance matrix	27
5.2 Incorporating non-linear loads.....	28
5.3 Validation of small-signal stability framework.....	29
5.4 Incorporating IBR black box models in small signal analysis.....	31
6 Small signal stability of synthetic NEM network with IBRs	37
6.1 Operating point and data selection.....	37
6.2 Analysis with white box IBR models - GFLs/GFMs	38
6.3 Impact of Load Modelling.....	41
6.4 Figure 36 NEM Network Simulation with Constant Admittance Loads Incorporating blackbox IBR models in the network analysis.....	42
6.5 Conclusions.....	47
7 Impact of current limits on IBR admittance characteristics	49
8 Conclusion and future work	55
Appendix A Analytical models and parameters.....	57

Figures

Figure 1 OP influence on the admittance frequency responses of the VSG-based GFMI model... 5

Figure 2 The methodology followed in the project 8

Figure 5 Process for comparing the performance of the two prediction algorithms 11

Figure 6 Example of predicted and expected admittance for the first IBR. ‘an’ and ‘dd’ refer to the APM and DDPM respectively and ‘M’ is the training data size. The right most number in each legend label is the goodness of fit of the prediction against the expected value. The operating point is $P=0.102$ pu, $Q=-0.302$ pu, and $V=1.058$ pu 12

Figure 7 Example of predicted and expected admittance for the second IBR. ‘an’ and ‘dd’ refer to the APM and DDM respectively and ‘M’ is the training data size. The right most number in each legend label is the goodness of fit of the prediction against the expected value. The operating point is $P=0.738$ pu, $Q=-0.336$ pu, and $V=0.910$ pu 12

Figure 8 Aggregate goodness of fit histograms for the first IBR model. ‘an’ and ‘dd’ refer to the APM and DDPM respectively and ‘M’ is the training data size. Note that the goodness of fit is presented in a logarithm axis..... 13

Figure 9 Aggregate goodness of fit histograms for the second IBR model. ‘an’ and ‘dd’ refer to the APM and DDPM respectively and ‘M’ is the training data size. Note that the goodness of fit is presented in a logarithm axis. 14

Figure 10 Goodness of fit statistics for (a) power-controlled GFLI and (b) PV-controlled showing the mean and standard deviations. The rows correspond to parameter variations, showing the multiple of the base parameter value. Columns consist of groups of four bars, each corresponding to Y_{dd} , Y_{qd} , Y_{dq} , Y_{qq} . Each group corresponds to a training data size, as indicated on the figure. The colour of the cells indicates the value of the goodness of fit metric. 16

Figure 11 Goodness of fit statistics for (a) VSG-controlled GFMI and (b) PI-controlled GFMI showing the mean and standard deviations. The structure and notation are the same as those in the previous figure. 17

Figure 12 A schematic of the PSCAD component modelling the control (left) and Simulink C Function block representing the IBR control (right) 18

Figure 13 The comparison of POC voltage and current waveforms of PSCAD and Simulink models for an active power ramp applied at 2.0s 19

Figure 14 The comparison of POC voltage and current waveforms of PSCAD and Simulink models for a voltage step of 0.05 p.u. applied at 6.01s..... 19

Figure 15 The comparison of POC voltage and current waveforms of PSCAD and Simulink models for a frequency step of 0.5 Hz applied at 6.0s 20

Figure 16 Flowchart of implementing APM prediction algorithm on identified black-box model. 22

Figure 17 Measurement points, grid, L1, and E1, of the black-box model..... 22

Figure 18 P, Q, V terminal responses with respect to their reference step changes at 2, 3, 4 s of the black-box model working in grid following mode.	23
Figure 19 P, Q, V terminal responses with respect to their reference step changes at 2, 3, 4 s of the black-box model working in grid forming mode	23
Figure 20 The distribution instance of training and testing OPs arrangement.	24
Figure 21 An overlay of one identified (thick red line) versus 200 predicted admittance (dot-dashed lines) of the black-box grid following inverter model at a randomly chosen OP.	25
Figure 22 The mean error rate of the admittance prediction on 17 testing cases of the black-box grid following inverter model.	25
Figure 23 An overlay of one identified (thick red line) versus 200 predicted admittance (dot-dashed lines) of the black-box grid forming model at a randomly chosen OP.....	26
Figure 24 The mean error rate of the admittance prediction on 17 testing cases of the black-box grid forming inverter model.....	26
Figure 25 Two-Area System Eigenvalues in Complex Plain	28
Figure 26 Step Response at Machine 32 Linearized Model (Left) Simulation (Right)	30
Figure 27 Step Response at Machine 37 Linearized Model (Left) Simulation (Right)	30
Figure 28 Step Response at Machine 34 Linearized Model (Left) Simulation (Right)	30
Figure 29 Eigenvalue Analysis of the IEEE 39 bus system.....	31
Figure 30 Comparison of the impedance characteristics obtained for the black box models for one of the IBRs against analytical small signal model	32
Figure 31 The input frequency data obtained from admittance prediction method/frequency scan compared with the vector fitted model for one IBR	33
Figure 32 Comparison of the impedance characteristics obtained for the black box models for one of the IBRs against analytical small signal model - different scan reference location	34
Figure 33 Vector fitted model based on the data from frequency scans/admittance prediction method compared with the analytical IBR small signal model, over a large frequency range	35
Figure 32 An approximate representation of the synthetic NEM network on the map of Australia	37
Figure 35 Time domain simulation results for a load trip - (a) when all IBRs have GFL controls and (b) when a select number of IBRs have GFM controls for the selected peak load (hour=19) operating point	38
Figure 33 Linearized System SG-GFL IBR Speeds Impulse Response (for IBRs Speed is the PLL integrator state).....	39
Figure 34 Linearized System SG-IBR Speeds Impulse Response.....	41
Figure 35 Linearized System SG-IBR Speeds Impulse Response with all loads represented as constant impedance.....	41
Figure 36 Linearized System SG-IBR Speeds Impulse Response with GFM Plants	42

6.4 Figure 36 NEM Network Simulation with Constant Admittance Loads Incorporating blackbox IBR models in the network analysis.....	42
Figure 37 Expected versus predicted impedance based on admittance prediction method.....	43
Figure 38 Vector fitting the qd term without allowing a pole with positive real value (a) and allowing a positive real value (b)	44
Figure 39 Vector fitted model compared with the input frequency characteristics for an IBR model	44
Figure 40 The frequency response of the vector fitted model compared with the analytical small signal model over a wide range of frequencies	45
Figure 41 A comparison of the poles of the open loop fitted model of the IBR and the open loop small signal analytical model of the IBR.....	45
Figure 44 Closed Loops Poles of System with Analytical and Identified Models	47
Figure 42: Single line Diagram of Kundur's Two Area System [9].....	49
Figure 43: Eigenvalues for Case 1.	50
Figure 44: Zoomed in comparison of eigenvalues	51
Figure 45: Eigenvalues when $k_{iPLL} = 50$, and k_{pPLL} is varied from 2 to 30 (IBR not operating at its current limit)	52
Figure 46: Eigenvalues when $k_{iPLL} = 50$, and k_{pPLL} is varied from 2 to 30 (IBR operating at its current limit)	52
Figure 47: Eigenvalues when $k_{pPLL} = 2$, and k_{iPLL} is varied from 50 to 1350 (IBR not operating at its current limit)	53
Figure 48: Eigenvalues when $k_{pPLL} = 2$, and k_{iPLL} is varied from 50 to 1350 (IBR operating at its current limit)	53
Figure 49: Eigenvalues for Case 3 varying k_p , a) not at limit b) at limit	54
Figure 50: Eigenvalues for Case 3 varying k_i , a) not at limit b) at limit.....	54
Figure 51: Eigenvalues for Case 4 varying k_i , a) not at limit b) at limit.....	54
Apx Figure A.1 Structure used for the generic GFLI analytical model. The loop marked CQ represents either a power controlled or voltage controlled (with Q_e and Q^* replaced with V_e and V^* respectively) GFLI.....	57
Apx Figure A.2 Structure used for the generic GFMI analytical model. The loops marked CP and CQ represent either} a VSG or PI-based power-controlled GFMI.....	57

Tables

Table 2 A comparison of modes for two area system incorporating non-linear loads between the small signal framework and reference values from literature.....	29
---------------------------------------------------------------------------------------------------------------------------------------------------------------	----

Table 3 The load, generation and interarea flows in different areas of the synthetic NEM network for the selected operating point 38

Table 3 IBR buses with lowest available MVA identified in the previous stage of the project, and the participation factors of these IBRs in the unstable mode 40

Table 4 A comparison of the fitted and analytical models in terms of the SCR value exhibiting unstable behavior 46

Table 5: Cases studied..... 50

Apx Table A.1 GFLI basecase parameter values..... 57

Apx Table A.2 GFMI basecase parameter values..... 57

Acknowledgments

The research presented in this report was funded by CSIRO, Australia's national science agency, and carried out as part of CSIRO's contribution to the initiatives of the Global Power System Transformation (GPST) Consortium. This research supports Australia's transition to a stable, secure and affordable power system and contributes to critical research identified by the Consortium required to accelerate the decarbonisation of our electricity grid. More details can be found at <https://www.csiro.au/en/research/technology-space/energy/G-PST-Research-Roadmap>.

The team would also like to acknowledge the valuable feedback and inputs from CSIRO and AEMO subject matter experts throughout the course of the project.

Executive summary

With the large growth in the share of inverter-based resources (IBRs) in the Australian power system, one aspect important for ensuring stable operation of the Australian power system is evaluating the system stability and stability margin in the small signal domain, considering the IBRs connected to the system. In the research roadmap submitted to CSIRO “Australian Research Planning for Global Power Systems Transformation research roadmap around Stability Tools and Methods”, ‘stability margin evaluation’ and ‘small signal stability screening methods’ were identified as two critical research topics; this stage of the project aims to continue to address these two research topics.

When evaluating the small signal stability involving IBRs, two approaches are commonly adopted. A linear system analysis can be performed using the IBR control structure, which can yield an insight into the IBR states participating in different oscillatory/unstable modes, thus providing key understanding into the potential pathways to ensure stability. However, such an approach is often not possible when blackbox models are made available to the network operators by the IBR original equipment manufacturers, where the detailed control structure is not available. In such a case, a frequency domain scan/model fitting approach can be used to incorporate the IBR model in small signal stability evaluation.

In the previous stage of the project (Stage 2: 2022-2023), two (data driven and analytical prediction) algorithms were developed to estimate the impedance characteristics of IBRs across a wide range of operating points. In this Stage 3: 2023-2024 project, the first broad objective is to enhance this approach: thus, the two algorithms are compared for IBR models with different control architectures and different operating points and control parameters. The accuracy of estimated impedance is compared, and it is found that the analytical prediction algorithm results in a better accuracy for all models tested. Further, a ‘black box’ IBR model is created and utilized to test the performance of the analytical prediction method when the exact IBR control structure is not known.

A second broad objective of this Stage 3 work is to perform a small signal stability analysis of a large network using positive sequence network model and to utilize the predicted impedance characteristics of IBRs from the first objective. The impact of the approximation of using a positive sequence network admittance model is tested for a small network. A small signal stability framework is utilized for a synthetic network model representing the area served by the National Electricity Market (NEM) with more than 2000 buses. The framework is validated using standard small network models and scaled for the larger network model including IBRs. It is expected that this approach will allow for conduction of stability analysis with blackbox dynamic models.

In relation to the 2021 Topic 2 Research Roadmap, the work done in this project addresses the critical topics listed below and advances the work by the respective percentage amount:

- Stability margin evaluation (Critical topic) – 60%
- Small signal stability screening methods (Critical topic) – 60%

In addition, the work done in this project also addresses the high priority topic '7. Modelling and model validation' and advances the work by 25%.

1 Introduction

With the large growth in the share of inverter-based resources (IBRs) in the Australian power system, one aspect important for ensuring stable operation of the Australian power system is evaluating the system stability and stability margin in the small signal domain, considering the IBRs connected to the system. In the research roadmap submitted to CSIRO 'Australian Research Planning for Global Power Systems Transformation research roadmap around Stability Tools and Methods' [1], stability margin evaluation and small signal stability screening methods were identified as two critical research topics; this stage of the project aims to address these two research topics.

When evaluating the small signal stability involving IBRs, there are commonly two approaches that are possible: a linear system analysis using the IBR control structure, which can yield an insight into the IBR states participating in different oscillatory/unstable modes, thus providing key understanding into the potential pathways to ensure stability. However, such an approach is often not possible when blackbox models are made available to the network operators by the IBR original equipment manufacturers (OEMs), where the detailed control structure is not available. In such a case, a frequency domain scan/model fitting approach can be used to incorporate the IBR model in small signal stability evaluation. However, there are a lot of practical challenges in utilizing frequency domain scan/model fitting techniques in practice. One key challenge here is that the small signal estimated impedance model thus calculated by such techniques (or by modelling the IBR control structure in detail and using linear system analysis) is valid in a small operating region around the operating point at which the measurements/simulations were conducted to estimate the IBR impedance model. Paired with the time-intensive nature of the frequency scan/model fitting approach, it may not be practical to estimate the IBR impedance model at every operating point for all IBRs in a system with a large number of IBRs such as the Australian power system.

To tackle this aspect, in the previous stage of the project, two methods were developed to estimate the IBR impedance characteristics at any operating point. Even with such methods, it is beneficial to reduce the number of operating points at which frequency scan operation must be performed to tune/train the methods to achieve a good accuracy in a wide array of operating points. Hence, one of the aims of the project in this stage was to further improve the methods developed in the previous stage to find out the impact of the number of operating points as well as IBR parameters on the accuracy of the methods. Since one of the key benefits of this approach is its applicability to black box IBR models, a black box IBR model was created to test the impedance model estimation techniques.

Small signal stability analysis is one of the standard techniques used by power system engineers for identifying potential unstable grid conditions. For a screening/identification of unstable/stable behaviour using small signal techniques for a given network operating point, the entire circuit may be needed to be modelled, with IBR devices represented in detail. For large circuits involving numerous IBRs, a systematic framework to represent the entire network in small-signal stability domain is used. However, the existing small signal analysis framework relies on having access to

and representing different devices including synchronous machines and IBRs in detail including the control block diagrams. With blackbox IBR models, such approach may require modifications. The systematic modelling approach used in this project is designed so that estimated impedance models from IBRs may be used in the place of actual IBR models.

IBRs are different from other resources such as synchronous generators in that they limit the current to a certain maximum value. When an IBR is operating at the current limit, its control structure and response might be very different from when it is operating at another operating point where the current limits are not binding. Hence, another aim of this project is to study the impact of current limits on the small signal response of IBRs and its impact on the small signal stability.

The Australian power system is recognized to have had a tremendous increase in the shares of IBRs and distributed energy resources (DERs), and such increase is expected to continue in the near future. With the increased penetration of IBRs in a power system, the oscillatory behaviour of the system is expected to change. The change in the oscillatory characteristics can be fundamentally related to the change in modes in the network. A network with rotating machines has electromechanical modes that dominate. Whereas with an increase in IBRs, depending on the bandwidth of control, different ranges of the oscillatory spectrum can equally dominate. Slower IBR controls can impact electromechanical modes, while faster IBR controls can interact with higher frequency dynamics (including electromagnetic modes), the network, or other controls operating in that range. This can bring about interactions on a much faster time scale. Thus, to allow for efficient operation of the network, it will be beneficial to characterize the oscillation characteristics at any operating point, especially with the increased uncertainty of variable generation.

Through this research effort, overall system stability assessment along with an accurate plant level IBR impedance prediction model can allow the network operators to have a clearer picture about the system stability for each operating point. The added insights from the small signal stability and oscillation modes for a network as a result of this research can potentially also shorten the connection cost for a new IBR, thereby encouraging more IBR integration. While these issues are relevant for the global energy sector as a whole, the pioneering nature of Australia's energy transition informed by its high scale and speed, leads these to have added relevance for the Australian scenario.

1.1 Relation to Research Roadmap

The research carried out in this stage is related to the following open research questions raised from the Topic 2 research roadmap document [1] (the subsection number and question numbers from the document are given in parentheses):

- Is it possible to evaluate non-linear stability margins using blackbox IBR models? Here, non-linear refers to the large signal behaviour of the IBR. Blackbox models more closely reflect the actual device behaviour under different conditions. A blackbox model is also expected to capture the dynamics of an IBR over a wider frequency range. However, research would need to be done to evaluate whether a non-simulation based analytical process can be used to evaluate

the stability margins under varying network behaviour. (Roadmap subsection 4.2.1 open research question 1)

- How would stability properties of other sources in the network be represented when designing an IBR plant? (Roadmap subsection 4.2.1 open research question 3)
- Would it be possible to efficiently evaluate small signal modes and stability profile with black box models? (Roadmap subsection 4.2.1 open research question 4)
- Identification of procedures to use impedance-based methods for stability screening and screening of converter driven stability risks. The methods and practices should be simple and yet reasonably accurate and aimed at reducing the total number of scenarios that need to be investigated with the use of detailed EMT time domain simulations. (Roadmap subsection 4.2.2 open research question 1)
- Documentation of methods that use extracted impedances to screen for risk of converter interactions as well as risk of instability. (Roadmap subsection 4.2.2 open research question 2)
- The use of linear frequency domain methods, such as linear models and eigenvalue analysis is another area that could benefit from additional research. It is well understood that linear methods can be used as an additional tool for the evaluation of some of the converter driven instabilities mentioned in this document. However, detailed linearized models for IBRs is not something that is widely currently available in the industry. While some commercial applications for linear/small signal analysis exist, those mainly account for models used to study electromechanical modes, such as inter and intra area oscillations. To study faster control interactions, the tools and models used would have to account for the faster regulators that impact a lot of those control instabilities. To what extent linearized models of IBRs can capture some of these phenomena and how those models should be developed is another area that would require further investigation. (Roadmap subsection 4.2.2 open research question 4)
- Development of a multi-operating point small signal model (either impedance based or linearized state space). Here again, there should be close synergy with Topic 1 to develop a multi-operating point model that can also be easily interfaced with existing small signal stability tools used by transmission network service providers (TNSPs) and the system operator (AEMO) in Australia. (Roadmap subsection 4.2.2 open research question 5)

Specifically, the project has progressed work related to two critical topics identified in the research roadmap:

- Stability margin evaluation
- Small signal stability screening methods

For each of these topics, the percentages of the research that have been progressed are (in relation to the initial 2021 roadmap):

- Stability margin evaluation – 60%
- Small signal stability screening methods – 60%

In addition, the project has progressed work related to a high priority topic identified in the research roadmap ‘Modelling and model validation’ and for this topic, the percentage of research that has been progressed is (in relation to the initial 2021 roadmap) 25%.

1.2 Background work

1.2.1 Inverter admittance and operating point dependence of admittance estimation algorithms

The impedance (or admittance) of a system is defined as the transfer function from perturbations in current (or voltage) considered as inputs to the system and its response in voltage (or current) which is considered the output [2]. Figure 1 OP influence on the admittance frequency responses of the VSG-based GFMI model. The colour of the trace indicates different OPs, in no specific order.

shows admittance Bode plots of an IBR, whose structure is shown in Apx Figure A.2 in Appendix A . The admittances are represented in the DQ domain yielding four separate quantities (e.g. Y_{dd} , Y_{dq} , Y_{qd} , Y_{qq}). Each of these quantities (e.g. Y_{dd} , Y_{dq} , Y_{qd} , Y_{qq}) corresponds to a transfer function between voltage (input) and current (output) involving all combinations of the D and Q axes.

The curves in the figure are produced by varying the IBR terminal voltage between 0.9 pu and 1.1 pu, output active power between 0.0 pu and 1.0 pu and output reactive power between -0.5 pu and 0.5 pu. This reactive power range has been considered to allow for normal operation of the inverter prior to any disturbance. It is clear from the figure that the inverter's admittance along certain axes is operating point (OP) dependent, particularly and more significant for lower frequencies. Note that each curve's colour corresponds to a unique OP for visual clarity. The operating point dependency comes about due to non-linear control loops such as the outer loop controls. These have relatively low bandwidths – i.e., less than 10 Hz. The faster dynamics comprising the voltage control loop, current control loop and electrical resonances are linear in nature. Therefore, the operating point has no impact on their dynamics.

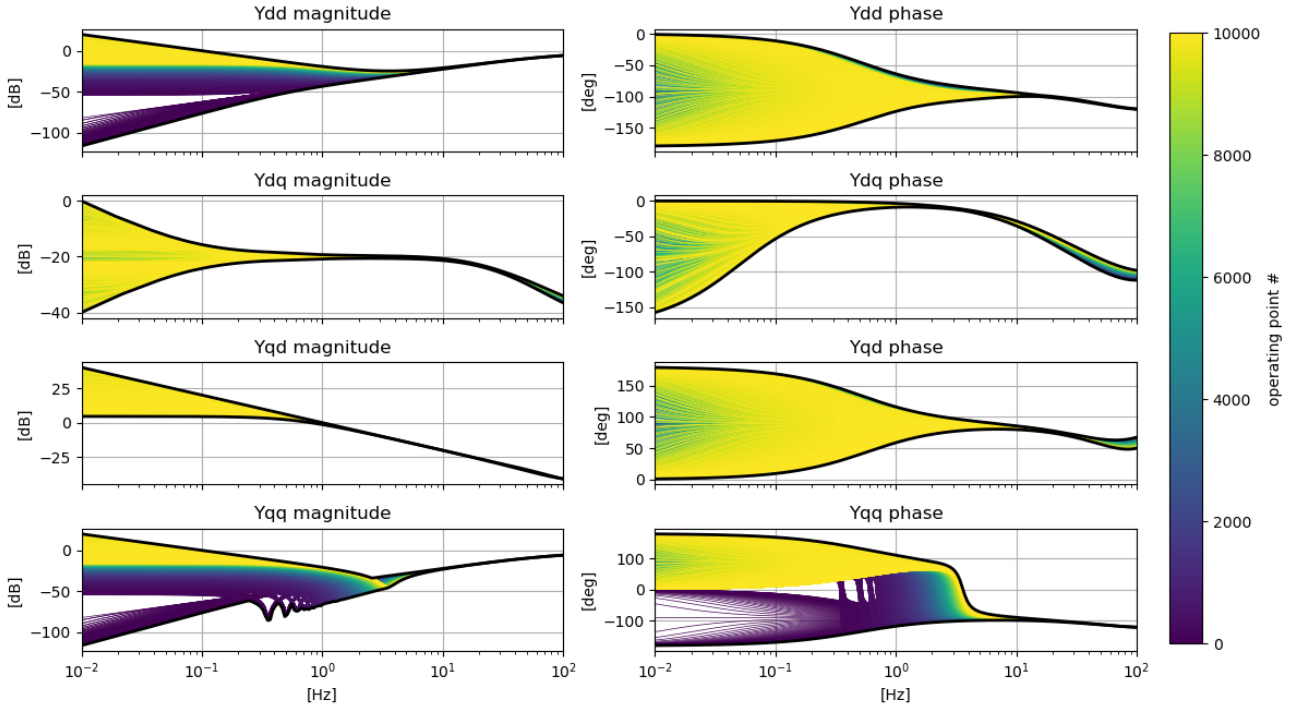


Figure 1 OP influence on the admittance frequency responses of the VSG-based GFMI model. The colour of the trace indicates different OPs, in no specific order.

1.2.2 Admittance prediction algorithms

The dependence of inverter admittance on the OP and the fact that the admittance of black-box models at each OP can only be determined through time consuming identification, which creates challenges for the use of such models for the purpose of evaluating the stability of a network. To deal with this challenge, in the previous stage, the team developed algorithms to predict inverter admittance at any OP based on a set of training data provided by the user. Two distinct algorithms were developed as part of this process: an Analytical Prediction Method (APM) and a Data Driven Prediction Method (DDPM).

The APM relies on a unified admittance model of the IBRs in the form of:

$$y_{\varepsilon}|_{s=j\omega_0} = \frac{\sum_{m=0}^M \sum_{i=0}^m v_d^i \left(\sum_{j=0}^{m-i} b_n^{\varepsilon} i_q^{j:m-i-j} \right)}{\sum_{m=0}^M \sum_{i=0}^m v_d^i \left(\sum_{j=0}^{m-i} a_n^{\varepsilon} i_q^{j:m-i-j} \right)} \quad (1)$$

Where $\varepsilon \in \{dd, dq, qd, qq\}$; ω_0 is the investigated frequency point; a_n^{ε} and b_n^{ε} represent the coefficients of the polynomial term $v_d^j i_q^{m-i-j}$ in the denominator and numerator respectively. The triplet (m, i, j) is indexed by:

$$n = \frac{m(m+1)(m+2)}{6} - \frac{i(i-2m-3)}{2} + j \quad (2)$$

An important parameter when applying the APM is the relative model order (M) and its optimal value depends on the inverter control structure. An inappropriate value can result in increased prediction errors. One method for determining this value is by increasing the model order (and corresponding training set size) until a required prediction error threshold is achieved.

In contrast, the DDPM utilizes a machine learning Gaussian process regression algorithm for admittance prediction. Though several data-driven prediction methods exist, this particular method was selected in the previous stage of this study for its robustness and reliability given limited training data size.

1.2.3 C code based blackbox IBR model

A generic C code based blackbox model was utilized in this project to test the admittance prediction algorithm. The C code based IBR model used for this project has been developed using a standardized code format being developed under the IEEE/CIGRE B4-82 working group and as a result, the code-based model can be seamlessly used in any EMT domain simulation software. Code based IBR model is tested and validated for both small and large signal performance [3].

1.2.4 Small-signal analysis framework

The framework that is utilized for the small-signal analysis in this work, was developed previously as part of EPRI's annual research portfolio, to address primarily control and general dynamic interactions during power system restoration [4].

Previous work at EPRI examined IBR-based blackstart for bulk transmission power systems. During that process, as more circuit elements, loads and generators came online, operating conditions and network topology changed drastically in each stage. The small signal framework was developed as part of this prior research effort to efficiently assess small-signal stability, identify what equipment contributes to each oscillatory mode and particularly what control loop is responsible. This allows efficient identification of drivers of instability and enables efficient control retuning, given that the responsible loops can be also identified. All this is achieved via eigen-analysis of the linearized power system model.

The framework was created to be able to work with positive sequence and EMT formulations of power systems and is utilized for this work.

1.2.5 Synthetic National Electricity Market network model

The team had also utilized a synthetic network model representing the area served by the National Electricity Market (NEM) [5] to develop a set of power flow cases to represent the evolution of the network over successive time periods (such as a 24-hour period), and carried out a preliminary time domain evaluation to identify any stability issues arising at these operating points. The time period corresponding to peak load is used in this stage as the base network operating point because it is one of the operating points that showed a tendency towards poorly damped oscillations.

For the considered synthetic network, 90% of generation from New South Wales and Victoria and 60% generation from Queensland were assumed to be IBRs. Further, the projected 2030 average diurnal demand variation from AEMO was used to create 24 hourly cases for this considered synthetic network.

The cases were enhanced using a voltage optimization tool from called Voltage Control Areas (VCA) Studio [6] and analysed potential weak grid conditions were evaluated using EPRI's Grid

Strength Assessment Tool [7]. Potential stability issues were identified by developing the dynamic data for the network and by performing initial dynamic stability analysis. It was found that when using grid following IBR controls (represented by generic REGCCU1/REECCU1 models using a Dynamic Linked Library (DLL) user model available from EPRI [8]) for all existing IBRs, for some hours the load trip resulted in oscillations, but when 35 new IBRs using the advanced grid forming controls (represented by GNRGFM models) were added to the system, these oscillations were eliminated. One of the network cases prepared using this process during the previous stage of project has been used in this stage to demonstrate the working/performance of the small signal stability framework described in this stage of the project.

1.3 Summary of work effort

In this stage of the project, the application of predicted IBR frequency domain characteristics in small signal analysis is investigated. For this purpose, the following work efforts are conducted:

- In the previous stage of the project, two methods to estimate the frequency domain admittance characteristics of IBRs for any operating point were developed. In this stage of the project, their effectiveness is compared by identifying the impact of the number of operating points used in the training data and the chosen operating points sufficient to generate training data.
- A small signal analysis framework is used with the positive sequence network admittance characteristic to identify any small signal unstable conditions and the devices/states that participate in oscillation modes that are unstable or poorly damped. This framework can then be used to identify the impact of IBRs on the system small signal stability and identify if a set of IBRs may be behaving in a cohesive or disruptive manner from the perspective of small signal stability.
- When the details of the controls for IBRs are not available, the frequency domain admittance/impedance characteristics of IBRs may be utilized to represent the IBR in a small signal stability assessment. A procedure to utilize the frequency domain impedance characteristics of IBR to form a state space model that can be incorporated into a small signal assessment is demonstrated in this stage of the project. Such models are incorporated into the small signal analysis of a large synthetic network model representing the area served by NEM as an illustrative example.
- An IBR is a current limited device, and as a result its stability at steady-state operating point may be influenced by such a current limit for particular operating points. The small signal characteristics of IBR may be impacted when operating at such a limit, and performing a preliminary evaluation of these impacts is another project aim.

2 Methodology followed in the project

The overall methodology from this project can be summarized in the form of a flowchart, depicting different work thrusts, as shown in Figure 2. More details of each work thrust are given below:

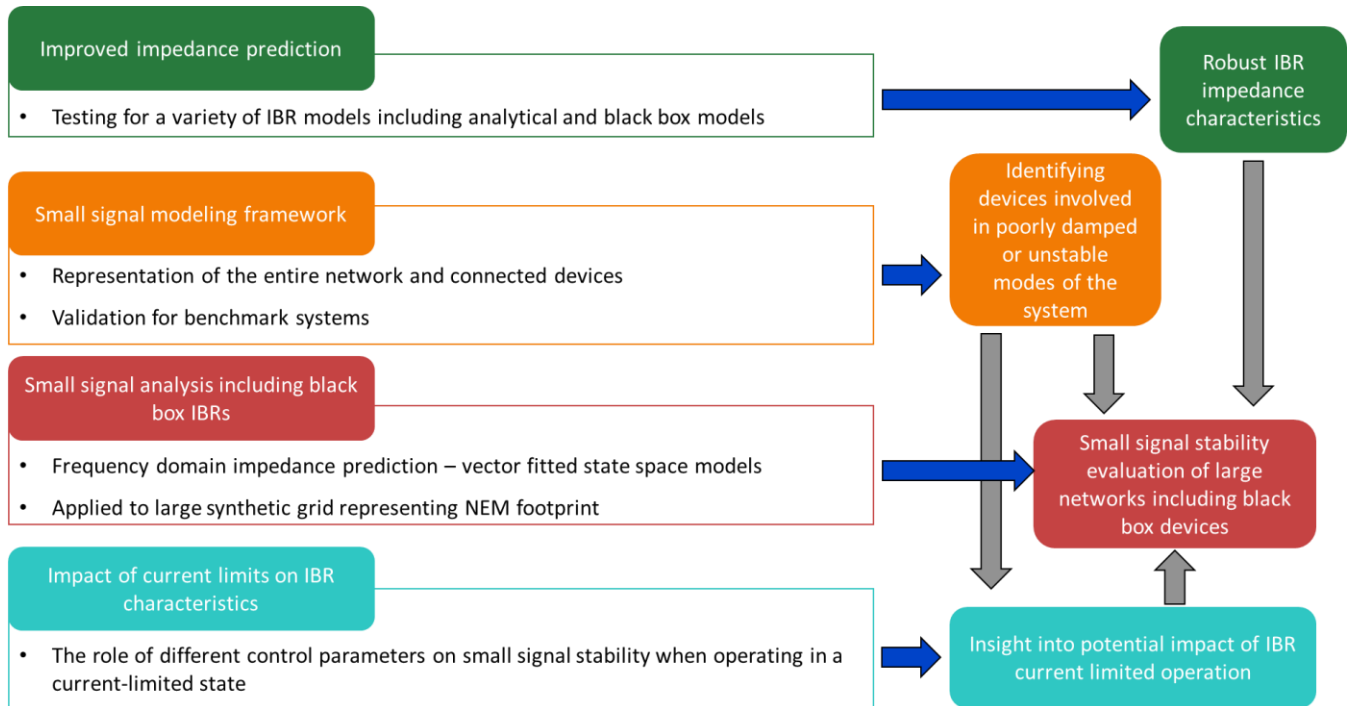


Figure 2 The methodology followed in the project

For the admittance prediction part of the project, the main objectives were to comprehensively compare and test the methods of estimating IBR admittance (analytical prediction method – APM and data driven prediction method – DDPM) and enhance it by assessing the impact of the number of training points and IBR control parameters for a variety of IBR configurations, using analytical inverter models.¹

In order to test the IBR admittance estimation process on a blackbox model where the IBR control structure is not known or assumed when performing the IBR admittance prediction process, a generic blackbox IBR model was utilized. For this purpose, an IBR control structure was represented as a dynamic linked library (DLL). Using this black box model, the performance of the APM model was validated. Such a validation allows for the development of a process to use the prediction method for real power systems.

In parallel, the small signal modelling framework was validated using two standard networks – a widely studied two area network [9] and IEEE 39 bus benchmark system [10]. In the case of two area network, the linearized models of the systems used positive sequence fundamental

¹ Analytical models are developed by deriving the fundamental equations which govern the dynamics of the inverter control its electrical components. Since the structure of these models are known they are considered to be white box type models.

frequency and EMT scale detailed network models. Further, for the small system, a preliminary investigation comparing the impact of two load models (constant impedance loads and constant current active, constant impedance reactive loads) was undertaken. For this system, the frequencies and eigenvalues were compared with the values available in standard textbooks (such as [9]) to validate the small signal model. For the 39 bus benchmark system, the step response from the small signal model was compared with a time domain simulation using Siemens PSS®E.

After the small signal framework was validated, it was extended to apply to an operating point for the synthetic NEM system. An operating point (hour) was selected for this purpose, and the powerflow case/dynamic data for that case from the previous stage of the project was utilized. For this operating point, an impulse response from the small signal model was compared with a Siemens PSS®E simulation where a very brief fault of 5 ms duration was applied to simulate the impulse disturbance.

The frequency domain impedance characteristics of IBRs obtained from the APM model applied to the blackbox IBR model were utilized to fit/form a state space model that approximates the IBR response. These state space models were validated against an analytical small signal model of the blackbox IBR, and were subsequently integrated to replace some of the IBR models in the synthetic NEM system to illustrate how such state space models based on frequency domain impedance characteristics might be used in a small signal study of a large network.

Lastly, the small signal model of an IBR was analysed to identify key changes in the dynamics when the current limits would become binding.

3 Comparison of IBR admittance estimation methods

The two estimation methods developed in the previous stage of this project have the objective of predicting admittance at new OPs based on known admittance at known OPs. By comparing the error between the predicted and expected values for each method, their performance for admittance prediction can be directly compared.

3.1 Method to compare performance

To undertake this assessment, the methodology shown in Figure 3 was adopted. This involved using a set of uniform random training and test OPs with IBR terminal quantities varied within the following range of values:

- voltage between 0.9 pu and 1.1 pu
- active power between 0.0 pu and 1.0 pu
- reactive power between -0.5 pu and 0.5 pu.

White-box analytical models of several IBRs were used to extract frequency domain admittances at these OPs to both train and to test the accuracy of each prediction method. Several training data sizes were tested (7, 19, 39)². These models are detailed in Appendix A . The process was repeated 5 times for each test case with 200 randomly generated OPs to test the prediction.

² The training sizes of 7, 19 and 39 were selected because they correspond to discrete APM model orders of 1, 2 and 3 respectively.

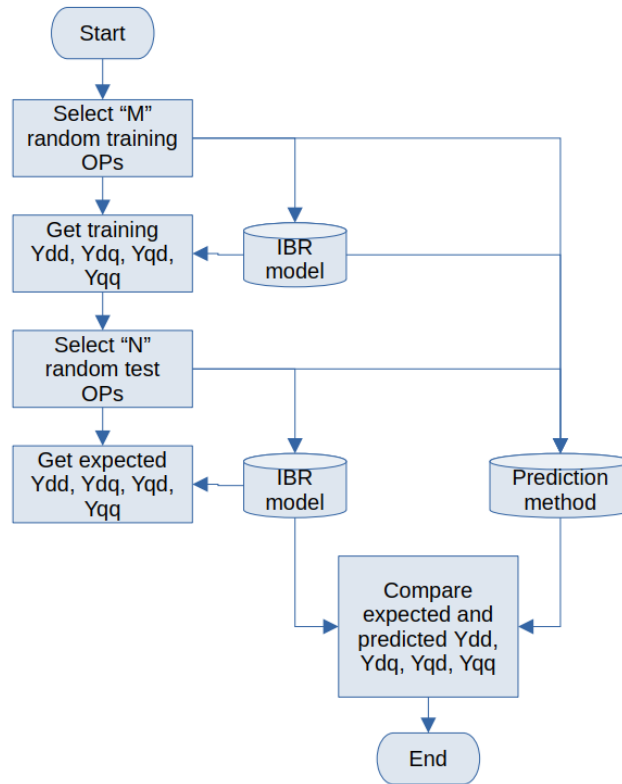


Figure 3 Process for comparing the performance of the two prediction algorithms

In addition to overlaying individual admittance results, an overall ‘goodness of fit’ statistic was calculated for each OP using the following equation to compare a reference array (the expected values) and the test data array (the predicted values):

$$err_{fit} = \frac{\|x_{ref} - x\|}{\|x_{ref} - \text{mean}(x_{ref})\|} \quad (3)$$

where the function $\|x\|$ represents the 2-norm of array of variable x , x is the test data, array x_{ref} is the reference data array, and $\text{mean}(a)$ indicates the average value of array a . The ‘goodness of fit’ metric yields a value of 0 for perfect alignment and a larger value for poorer alignment. For this comparative study, a goodness of fit value below approximately $10E-3$ is defined to be a very good fit result.

3.2 Comparison of the APM and DDPM

Test simulations to obtain expected and predicted admittance data were conducted on two distinct IBR models: a grid-forming inverter (GFMI) and a grid-following inverter (GFLI). These two structures represent most commonly studied and deployed IBRs. However, their admittances show different features due to differences in synchronization and terminal control strategies. The goodness of fit metric was calculated for each test OP (comparing the predicted admittance against the expected). An overlay of the expected and predicted admittance for one case is shown in Figure 4 and Figure 5. These overlay results already indicate that the APM can generate a much more accurate prediction compared with the DDPM given the same quantity of training data.

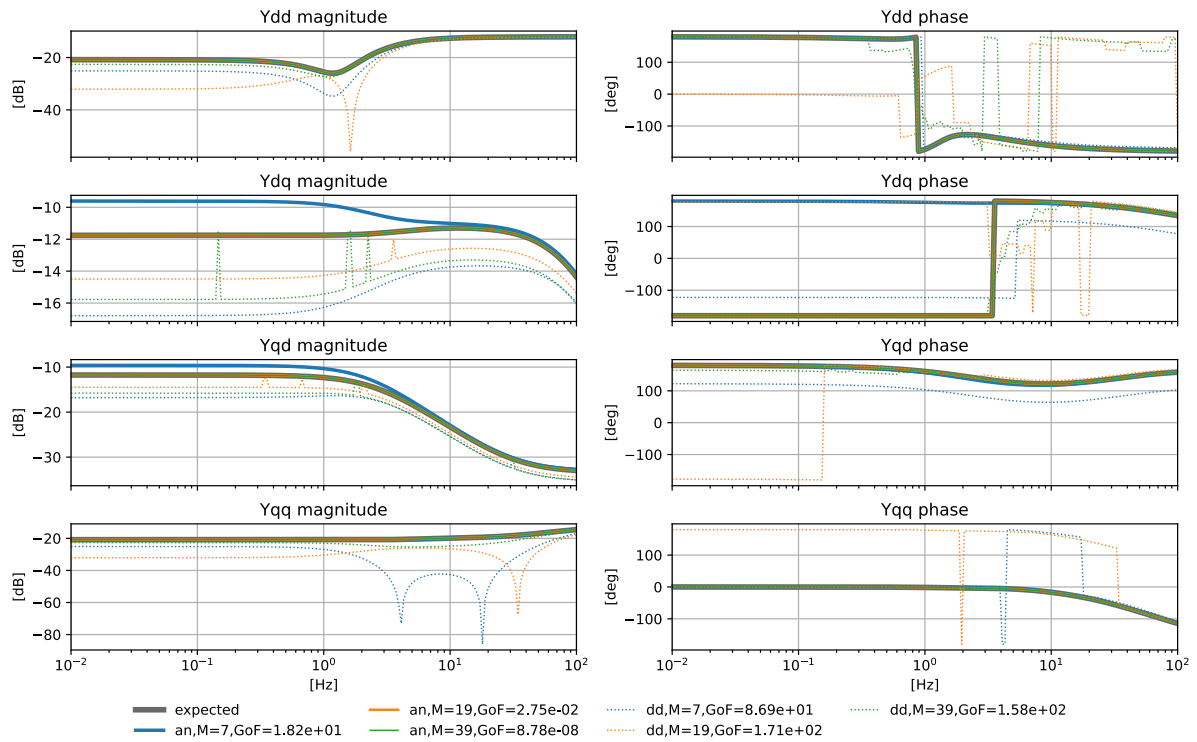


Figure 4 Example of predicted and expected admittance for the first IBR model. 'an' and 'dd' refer to the APM and DDPM respectively and 'M' is the training data size. The right most number in each legend label is the goodness of fit (GoF) of the prediction against the expected value. The operating point is $P=0.102$ pu, $Q=-0.302$ pu, and $V=1.058$ pu

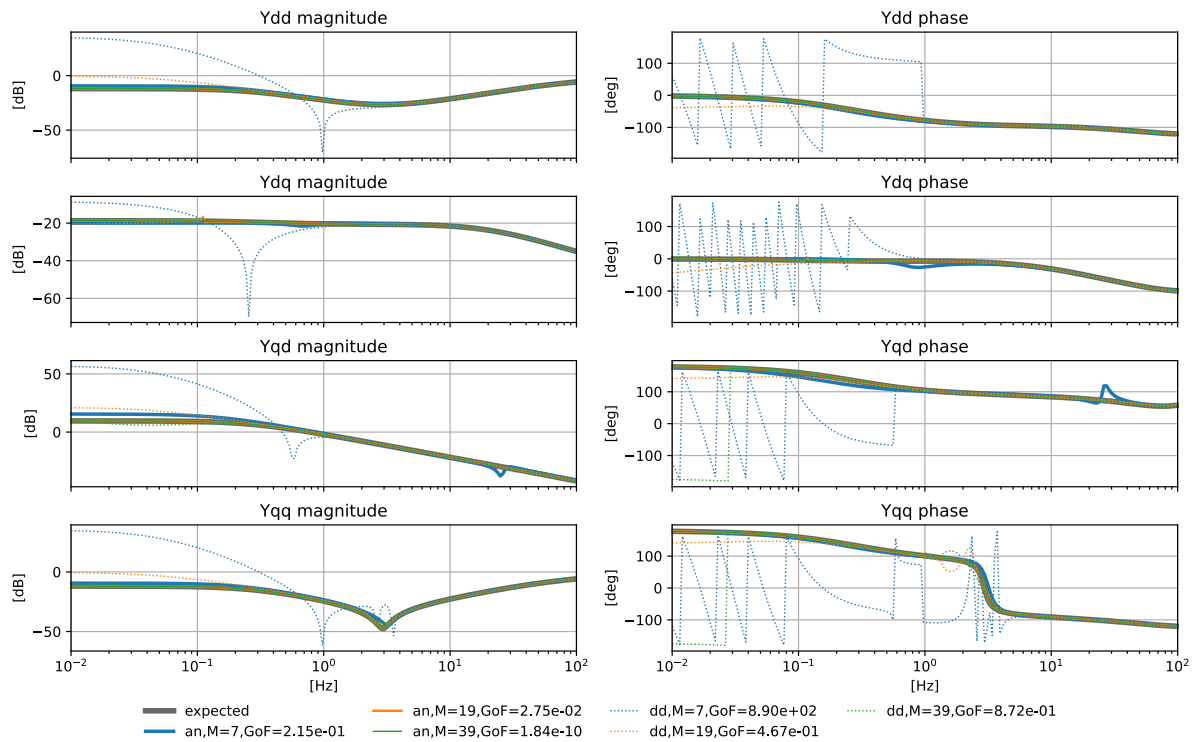


Figure 5 Example of predicted and expected admittance for the second IBR model. 'an' and 'dd' refer to the APM and DDM respectively and 'M' is the training data size. The right most number in each legend label is the goodness

of fit (GoF) of the prediction against the expected value. The operating point is $P=0.738$ pu, $Q=-0.336$ pu, and $V=0.910$ pu

To systematically compare the performance of the two methods across all the tests conducted, histograms of the goodness of fit metric were developed and are shown in Figure 6 and Figure 7. From these results, it can be observed that:

- As the training size is increased, the goodness of fit metric decreases indicating that the accuracy of the prediction increases.
- The goodness of fit metric is consistently and significantly higher for the DDPM compared to the APM. This indicates a poorer fit for the DDPM compared to the APM. This corroborates the result from Figure 4 and Figure 5 which show the DDPM performs very poorly.
- For the APM, though the goodness of fit continues to reduce in both cases with further increased training size, the increased accuracy may not be significant. Achieving goodness of fit results below 10^{-3} already produces accurate enough results.

These results demonstrate the superior performance of the APM and justify further investigation of this algorithm in the project.

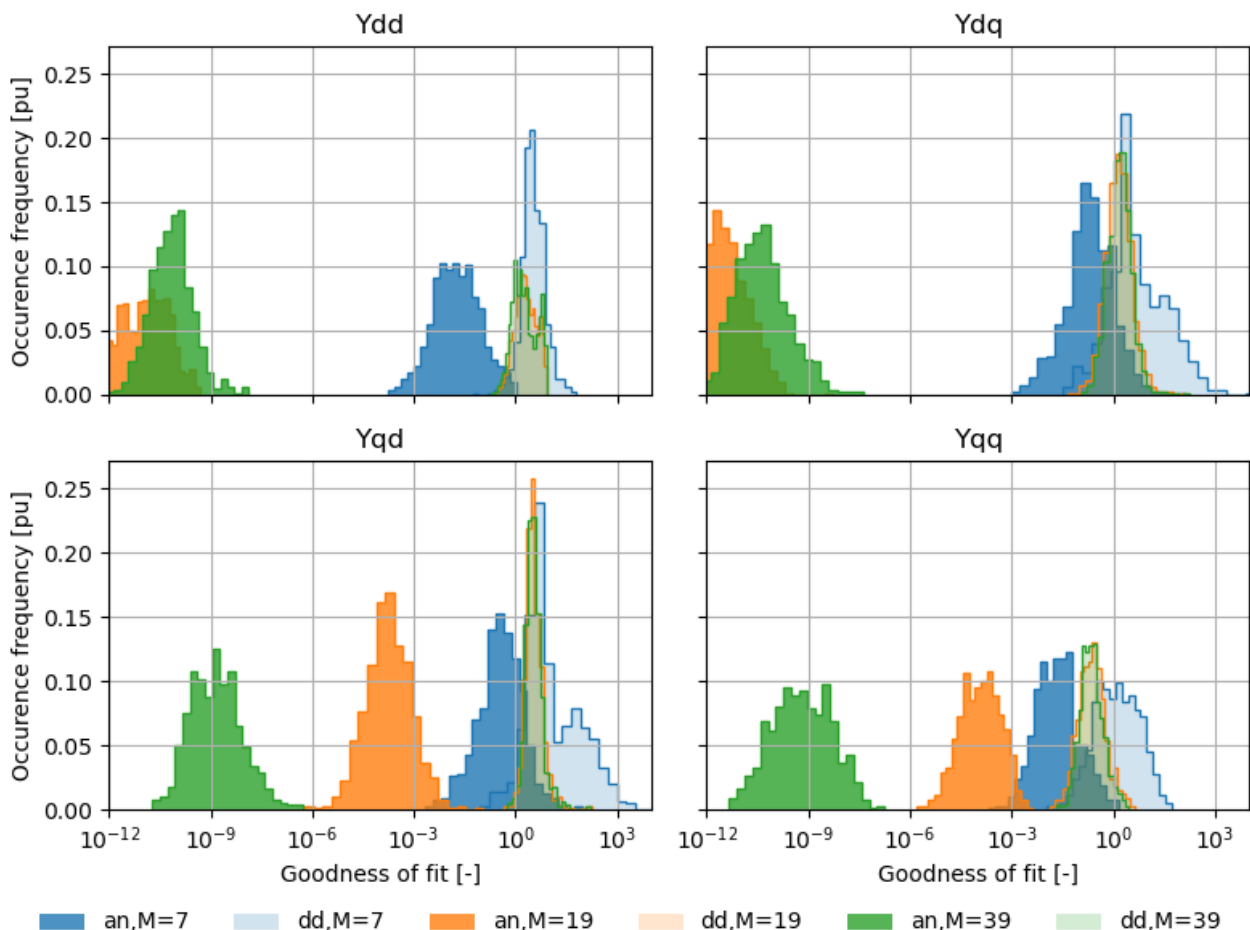


Figure 6 Aggregate goodness of fit histograms for the first IBR model. ‘an’ and ‘dd’ refer to the APM and DDPM respectively and ‘M’ is the training data size. Note that the goodness of fit is presented in a logarithm axis.

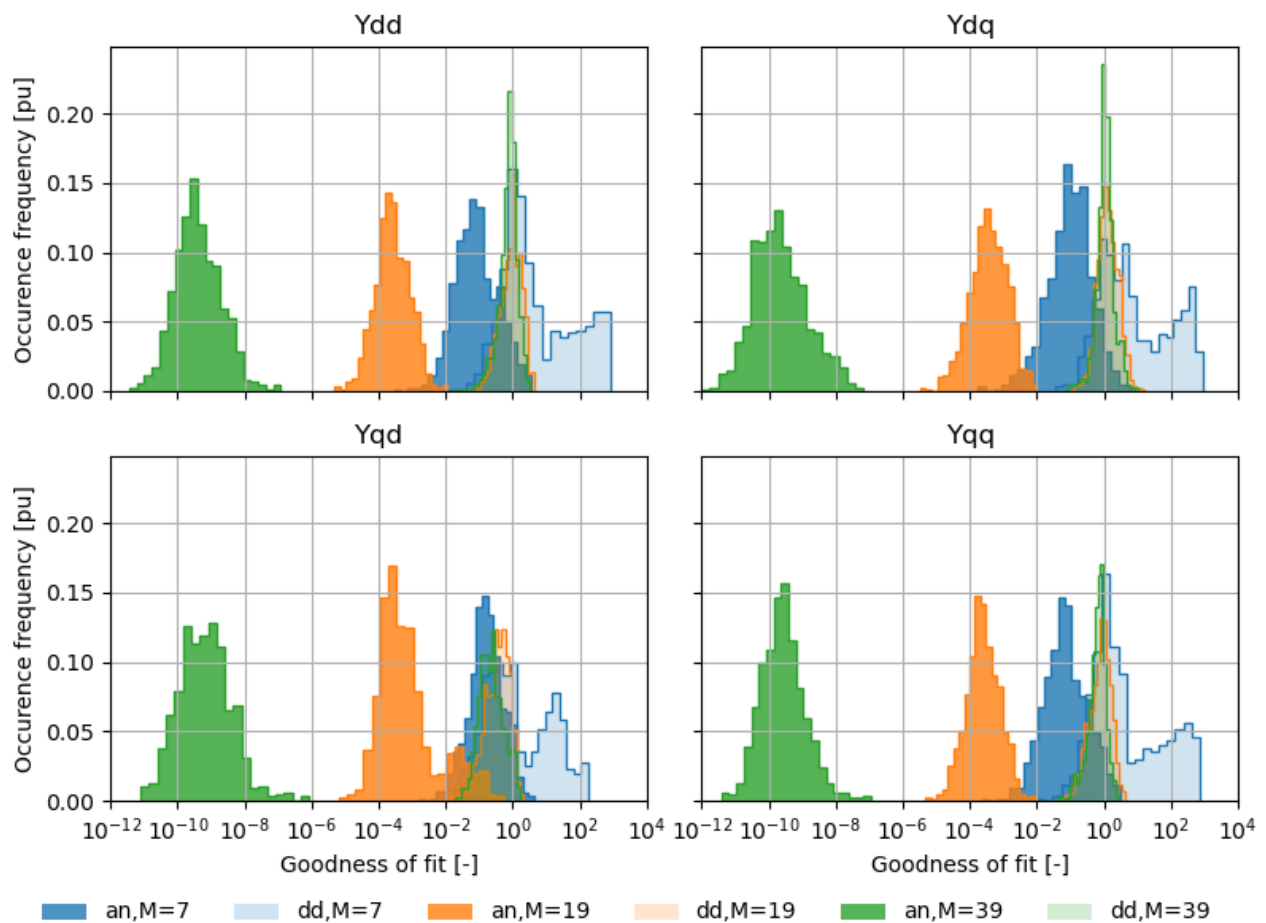


Figure 7 Aggregate goodness of fit histograms for the second IBR model. ‘an’ and ‘dd’ refer to the APM and DDPM respectively and ‘M’ is the training data size. Note that the goodness of fit is presented in a logarithm axis.

3.3 Investigation of the APM to inverter control structure and parameter sensitivities

This section details additional sensitivity analysis cases involving variations in model structure and parameters that were tested using only the APM.

Several IBR control structures were tested including:

- A power controlled GFLI and a voltage controlled GFLI.
- A VSG controlled GFMI and PI controlled GFMI.

Note that the purpose of these distinctions is to show that a couple of control structures were considered for each of the GFLI and GFMI. These distinctions do not matter for a blackbox model where control structure may not be known. For the GFLI control structures, variations were considered for the following control parameters:

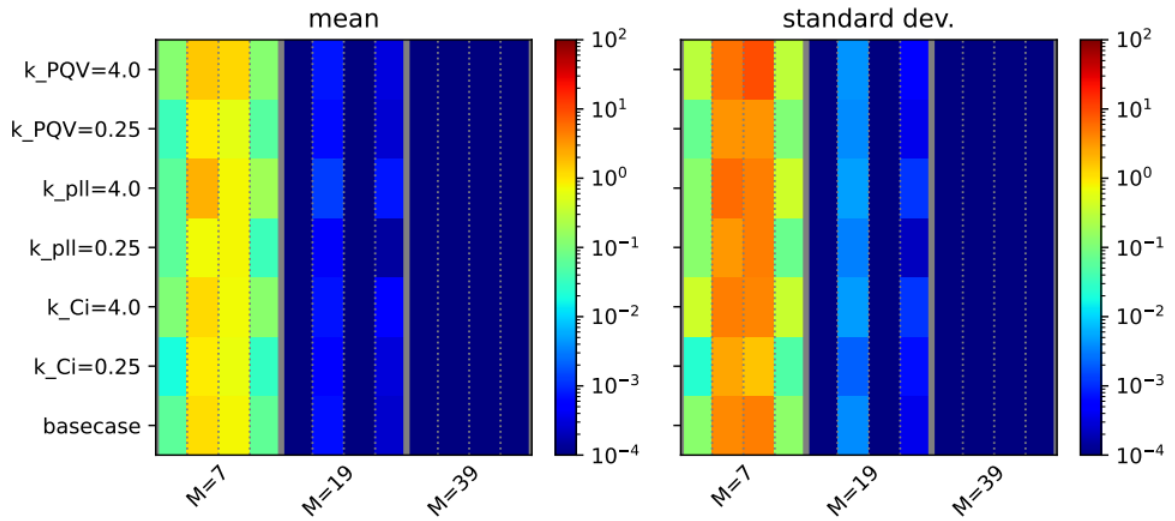
- Current controller bandwidth (k_{Ci}),
- PLL controller bandwidths (k_{pll}),
- P, Q or V outer loop controller bandwidth (k_{PQV}).

For the GFMI control structure on the other hand, variations were considered to the following parameters:

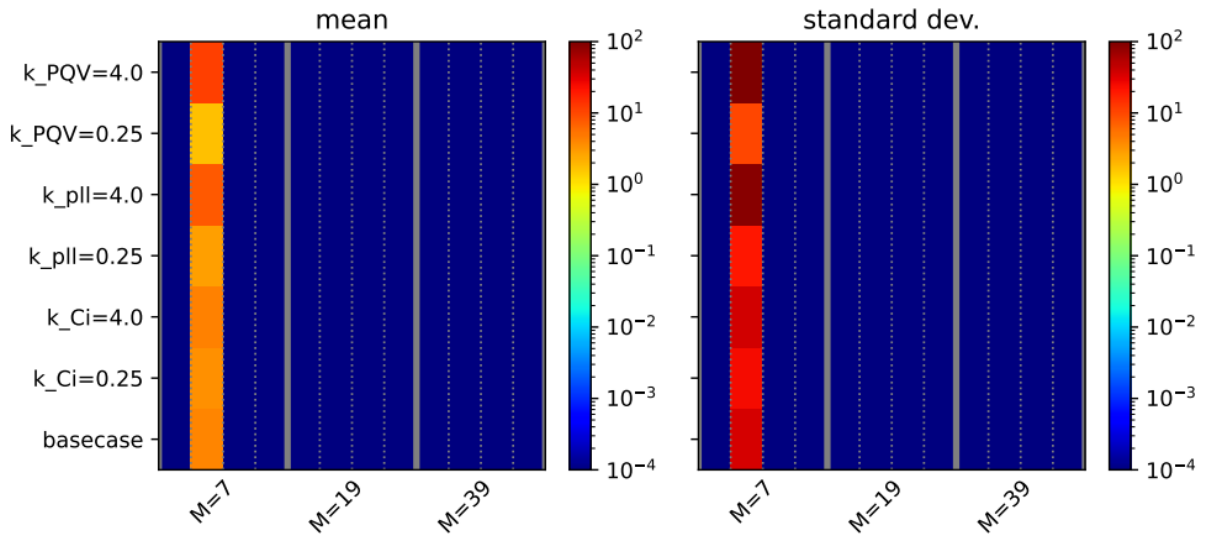
- Current controller bandwidth (k_i),
- Voltage controller bandwidth (k_v),
- For the VSG-GFMI, machine acceleration time constant (T_a), damping constant (K_D) and voltage droop constant (K_q),
- For the PI-GFMI, active power and reactive power controller bandwidths (k_{pi_P} , k_{pi_Q})

The results (see Figure 8 and Figure 9) show that the parameter sensitivities have some influence on the prediction accuracy. However, the training data size is much more impactful compared to the variation in parameters. With 19 training points, very low mean goodness of fit values are observed for both the GFLI control structures irrespective of parameter variations. For the GFMI structures, the mean goodness of fit was observed to be marginally above the 10^{-3} threshold with 19 training points. With 39 training points however, an extremely low goodness of fit result is achieved. These results indicate that for the control structures tested:

- 19 to 39 training points are adequate in obtaining accurate prediction results using the APM.
- For the set of tested control structures, it was found that the control structure was more influential on the minimum number of training points required to achieve a particular goodness of fit, rather than the control parameter.

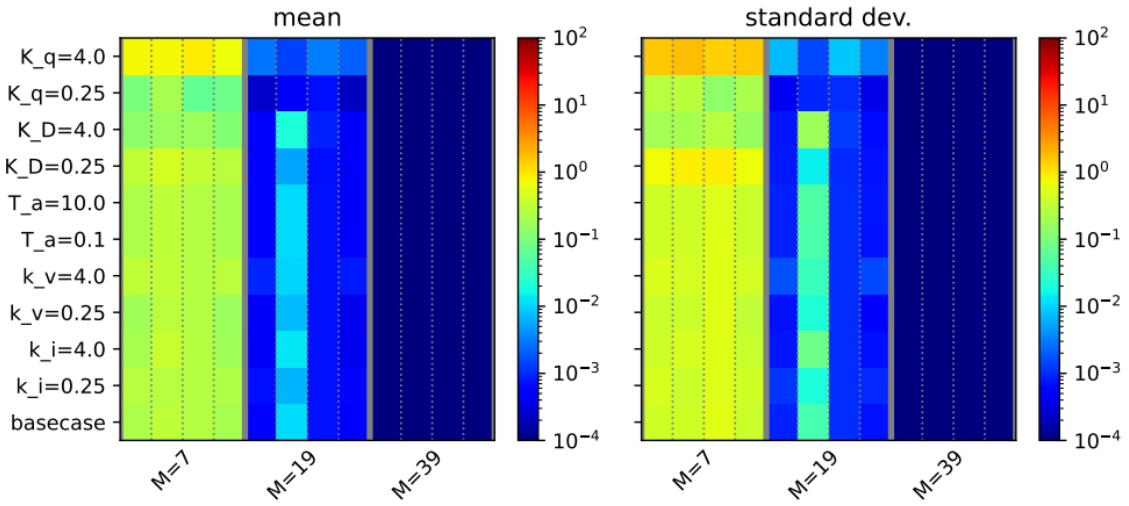


(a)

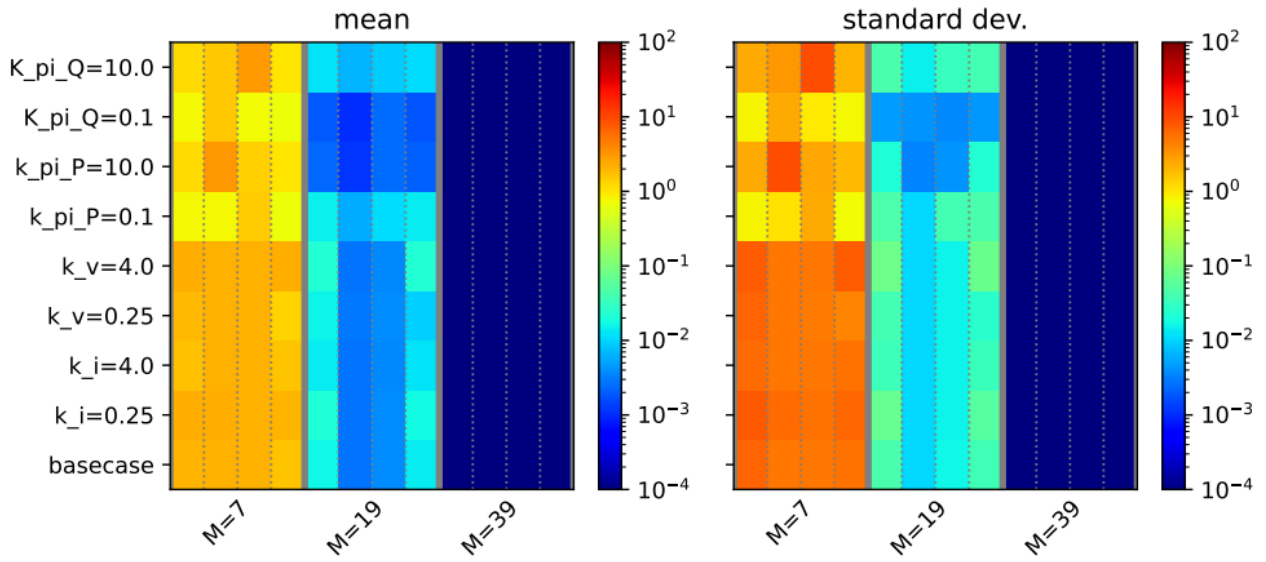


(b)

Figure 8 Goodness of fit statistics for (a) power-controlled GFLI and (b) PV-controlled showing the mean and standard deviations. The rows correspond to parameter variations, showing the multiple of the base parameter value. Columns consist of groups of four bars, each corresponding to Y_{dd} , Y_{qd} , Y_{dq} , Y_{qq} . Each group corresponds to a training data size, as indicated on the figure. The colour of the cells indicates the value of the goodness of fit metric.



(a)



(b)

Figure 9 Goodness of fit statistics for (a) VSG-controlled GFMI and (b) PI-controlled GFMI showing the mean and standard deviations. The structure and notation are the same as those in the previous figure.

4 Application of IBR admittance estimation method to a black box IBR model

4.1 Black box IBR model

Testing the admittance prediction algorithms with a blackbox IBR model will provide useful feedback and help improve the robustness of the admittance prediction algorithm. Hence, a blackbox model was developed by the team for the admittance prediction algorithm. The code for a previously developed blackbox model for PSCAD was utilized to create a consistent model for Simulink. This base model was a PSCAD model representing inverter-based resources (IBRs) developed as part of a prior project that models the IBR control using a dynamic linked library compiled from a code written in C based on the IEEE/CIGRE DLL standard currently under development [3]. Starting from the PSCAD model, a C-code based control block was used in Simulink with the same inputs, outputs and parameters as the original PSCAD model, and the actual control code was imported as a DLL, resulting in a blackbox model. A schematic of the original PSCAD block as well as created C Function block are shown in Figure 10. The rest of the components within the IBR such as the filter were also recreated in Simulink. More details of the process followed in creating this model are available in [11].

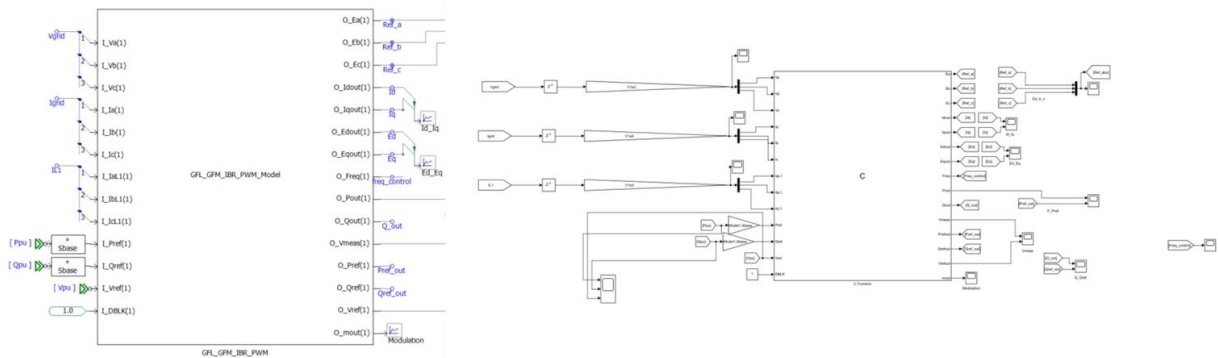


Figure 10 A schematic of the PSCAD component modelling the control (left) and Simulink C Function block representing the IBR control (right)

In order to test the models, they were connected to an ideal three-phase source behind an impedance ($SCR=6$, $X/R=10$), and the POC voltages and currents (at 33 kV) between the two models were compared for a steady-state active power ramp, a voltage step and a frequency step, as shown in Figure 11, Figure 12 and Figure 13, respectively. A good match between the POC currents and voltages indicates a good match between the models used in the two software platforms. While Figure 11 to Figure 13 are plotted for GFM mode, the POC currents and voltages were also found to match for the GFL mode.

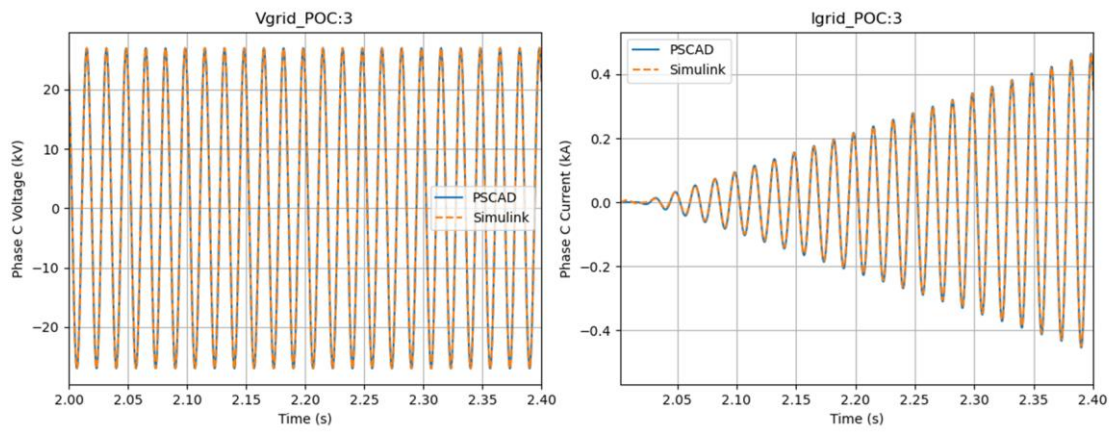


Figure 11 The comparison of POC voltage and current waveforms of PSCAD and Simulink models for an active power ramp applied at 2.0s

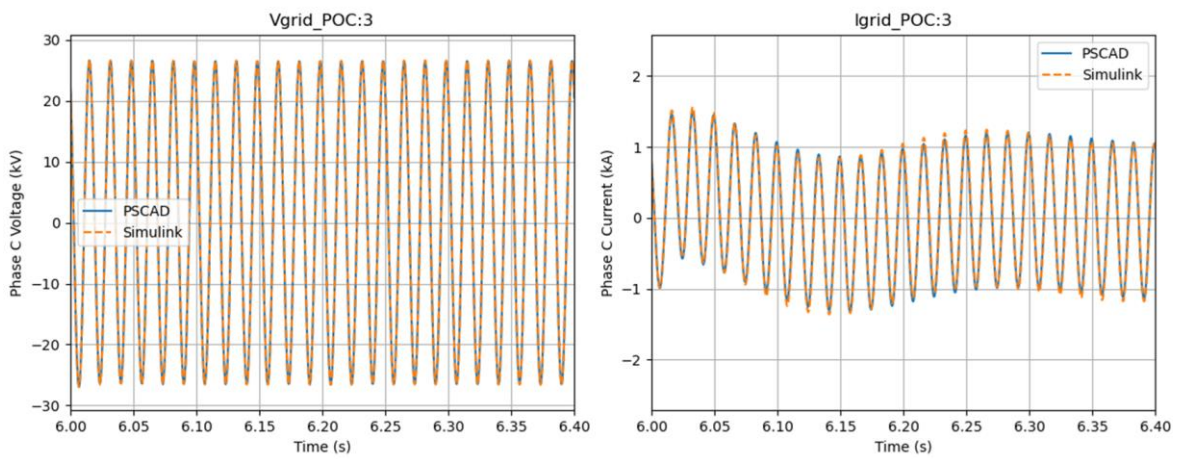


Figure 12 The comparison of POC voltage and current waveforms of PSCAD and Simulink models for a voltage step of 0.05 p.u. applied at 6.01s

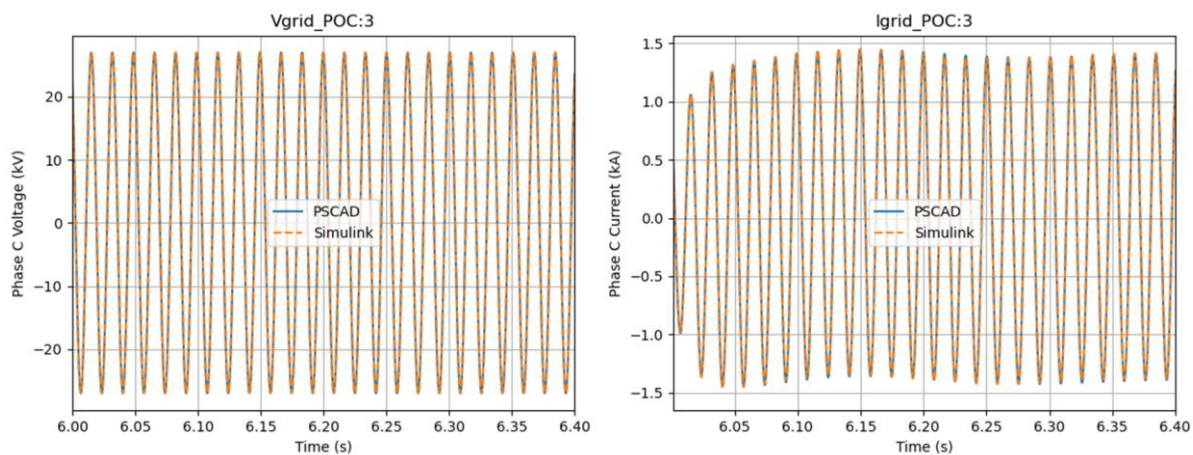


Figure 13 The comparison of POC voltage and current waveforms of PSCAD and Simulink models for a frequency step of 0.5 Hz applied at 6.0s

4.2 Application of admittance estimation methods

This section describes the application of the analytical admittance prediction method (APM) for the created black box IBR model. The Monte-Carlo method [12] is used to validate if APM gives consistent results. The following sections describe the testing procedures of how to prepare credibly identified data for the APM algorithm. After that, the prediction results are assessed for the black-box model working in both grid-following and grid forming mode.

4.2.1 Testing procedures

The procedures encompass several key stages: inverter control scope determination, admittance determination and dataset preparation, and prediction.

The initial step involves determining the control scope, a critical aspect as APM relies on the premise that the control scope of the inverter is predefined where an inverter tracks its voltage and power set-points on the circuit. An identification block is incorporated to ensure that any injected perturbation is promptly detected by the inverter's control system.

Subsequently, admittance is identified for the black-box model. This entails applying a series of sinusoidal perturbations at the point of connection and recording the circuit's response. Utilizing Discrete Fourier Transformation (DFT), signals corresponding to the injected frequencies are extracted. Admittance is then computed by dividing input and output quantities, a method elaborated in [13]. For a white box model, the admittance was identified directly from the analytical models and as a result, no perturbation methods were applied. Notably, for grid-following inverters, voltage perturbation serves as the input, while current perturbation constitutes the output. Conversely, for grid-forming inverters, the roles are reversed. If a model is found to behave in a different manner, the choice of input and output signals are reassessed. The selection process for operating points (OPs) aligns with the methodology outlined in Section II, ensuring that limiter elements within the inverter's control remain unaffected. Moreover,

perturbations are deliberately kept small to mitigate significant nonlinear behavior in the response.

The subsequent step involves determining the actual dq voltage and current quantities from the DFT applied to the time-series measurements, by extracting their DC components. This is necessitated by the inherent constraints of circuit theory, wherein voltage magnitude, real power, and reactive power cannot be simultaneously controlled. Following normalization of voltage and current, real and reactive power are calculated using prescribed equations, $P_e = -V_d I_d$ and $Q_e = V_d I_q$, given the negative current direction. The curve plot should look smooth in the frequency domain, as the identified admittance are resultant from continuous transfer function approximation.

To facilitate the creation of training and testing datasets, the admittance of the black-box model is scanned at 150 randomly selected OPs, within a frequency range of $\pm (1, 65)$ Hz deviation from the fundamental frequency, where OPs exert the most significant impact on dq domain admittance, as being illustrated in Section 1.2.1. Seventeen out of the 150 OPs are designated as the testing set to assess prediction accuracy, while the remaining 133 OPs constitute the training pool. From this pool, individual training OP sets are drawn to execute Monte-Carlo validation. This involves randomly selecting a training set comprising 19 points from the pool and executing prediction operations on the same 17 test OPs using APM, a process iterated 1000 times. The 150 OPs or 1000 iterations are chosen for Monte Carlo (MC) procedure that the combination of OPs for unknown OP prediction is far larger than the iteration numbers. For example, in the above case, the combination of 19 OPs from 133 OP pool gives the following approximate number of combinations possible of picking 19 OPs from the pool of 133 training OPs:

$$C(133,19) \approx 4.8 \times 10^{22} \gg 10^3$$

Subsequently, the prediction's efficacy is assessed. Figure 14 summarizes the procedure of the APM implementation on black-box model.

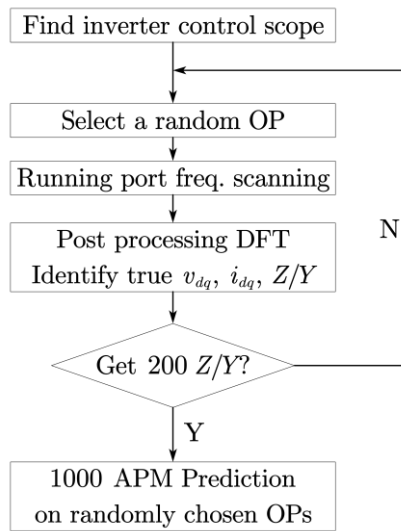


Figure 14 Flowchart of implementing APM prediction algorithm on identified black-box model.

4.2.2 Pre-requisite testing

APM is based on the assumption that the control scope of the inverter is known. It is vital to determine the scope of control. By applying a series of step changes on power/voltage set-points of the inverter, it is possible to determine which measurement point is tracking set-point references. Figure 15 shows three measurement points that are determined in the black-box model.

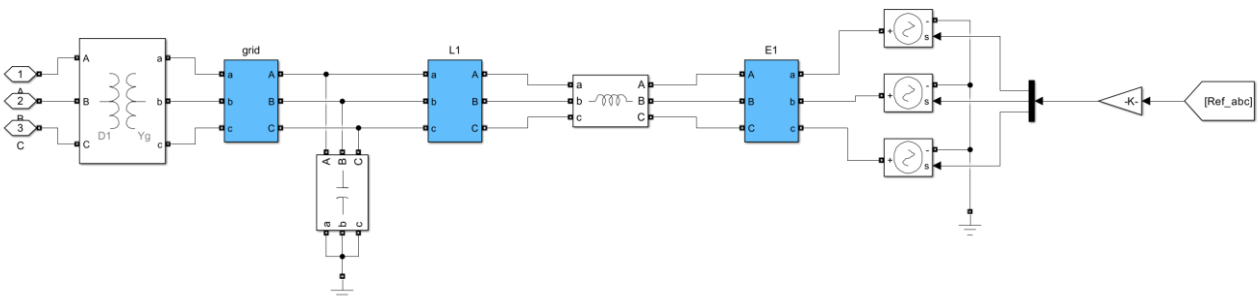


Figure 15 Measurement points, grid, L1, and E1, of the black-box model.

Figure 16 illustrates voltage, real power, and reactive power measurements obtained from the circuit when the inverter operates in grid-following mode. The plot reveals that the inverter effectively controls reactive power at point L1. Additionally, real power remains consistent across the point 'grid', point 'L1', and point 'E1' from Figure 15, voltage measurements deviate from the set-point references, indicating that grid-following mode primarily exerts control at point L1. If the blackbox grid following mode had voltage controller embedded in this control structure, there would be a difference in the output reactive power as compared to the reactive power control structure. The impact of this difference is to be analysed in future work.

Similarly, Figure 17 depicts measurements obtained when the inverter operates in grid-forming mode. Here, the inverter regulates voltage at both the grid and point L1. Notably, there exists a droop correlation between reactive power and voltage, which features a small deviation of the reactive power from its reference for balanced power sharing among inverter cluster. Given the unknown control structure, it is imperative to evaluate the impact of perturbation injection, where

GFLI is perturbed by its Point-of-Coupling (PoC) voltage, and GFMI is perturbed by its PoC current by recognizing GFLI as a voltage-controlled current source and GFMI as current controlled voltage source. Through an iterative process by replicating the measurement and finding the most relevant reference tracking point (as described through this and previous paragraph), it is determined that the GFMI controller effectively captures the current perturbing the capacitor voltage at point 'grid'.

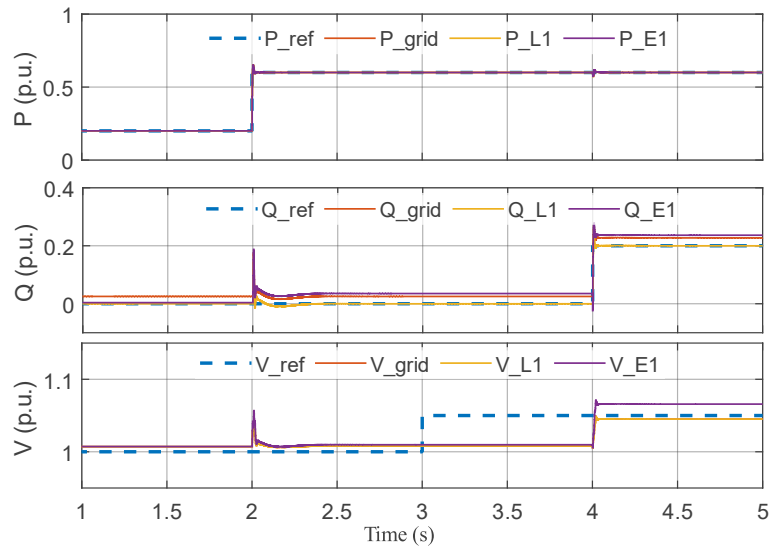


Figure 16 P, Q, V terminal responses with respect to their reference step changes at 2, 3, 4 s of the black-box model working in grid following mode.

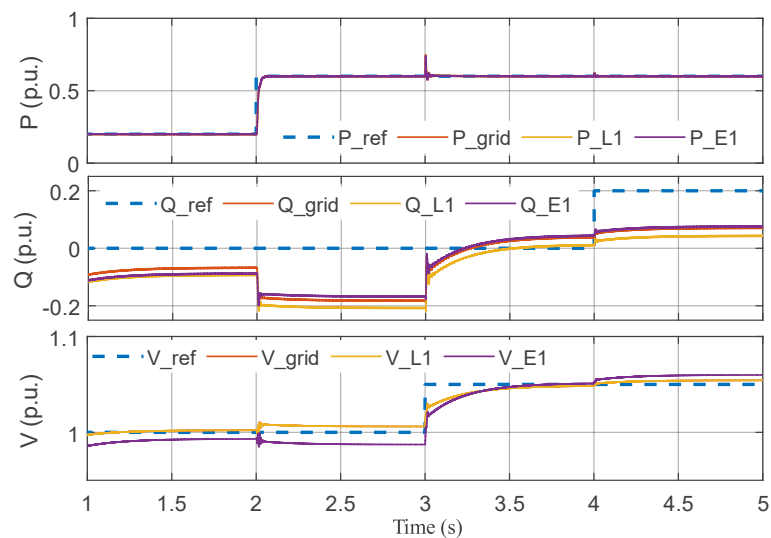


Figure 17 P, Q, V terminal responses with respect to their reference step changes at 2, 3, 4 s of the black-box model working in grid forming mode

4.2.3 Predicting Result Assessment

Figure 18 exemplifies the spread of training and testing tests arrangement of the OPs for an instance of test of the grid following inverter. In the OP space, points are spread randomly without clustering. Testing points are randomly chosen from the OP space. It assures the stochastic process of the prediction without bias.

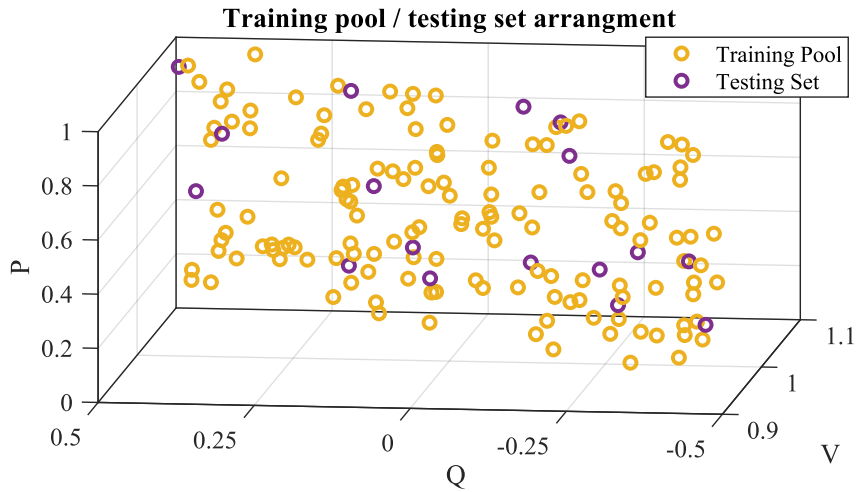


Figure 18 The distribution instance of training and testing OPs arrangement.

To quantify if the prediction is reliable, we define a successful prediction at a certain frequency f_i to first satisfy the distance criteria. This differs from (3) in that the absolute error deviates from the mean of the data set rather than the relative error deviating from an individual data point.

$$\|x_p^{f_i} - x_e^{f_i}\|_2 < \mu |x_e^{f_i}| \quad (4)$$

where $\mu = 0.1$ is the distance tolerance ratio, $x_p^{f_i}$ is the predicted admittance with respect to the expected value, $x_e^{f_i}$, at f_i . The value of μ is a subjective selection for this test. Secondly, a successful prediction also needs to satisfy the counting criteria that 90% of points in the frequency range should pass (4) on all four axes, i.e., dd, qd, dq, qq. If both criteria are satisfied, we consider this a successful prediction.

Grid-following Inverter testing results

Figure 19 exemplifies the identified admittance versus 200 out of 1000 predicted ones of the black-box model, which was configured as a GFLI. In this case, the predicted admittances mostly overlay on the measured admittance, verifying the feasibility of (1) for the black-box model that was tested. This demonstrates that the proposed APM is successful when used with this black-box model.

Figure 20 reflects the mean ratio of the wrongly predicted frequency-dependent admittance upon dd, qd, dq, qq elements in the predicted frequency range. The error rates of diagonal elements (dd, qq) are below 0.002, whereas the off-diagonal (dq, qd) error rates are below 0.03. It locates in the zone with relatively small magnitude. In addition, the cross-coupling effect of GFL is mostly induced by outer power exchange and synchronization, of which controllers work in lower frequency. All impedance predictions are well below the acceptance threshold, which is 0.1. Diagonal and off-diagonal elements may have frequency-dependent error tolerance for stability studies, which needs further investigation.

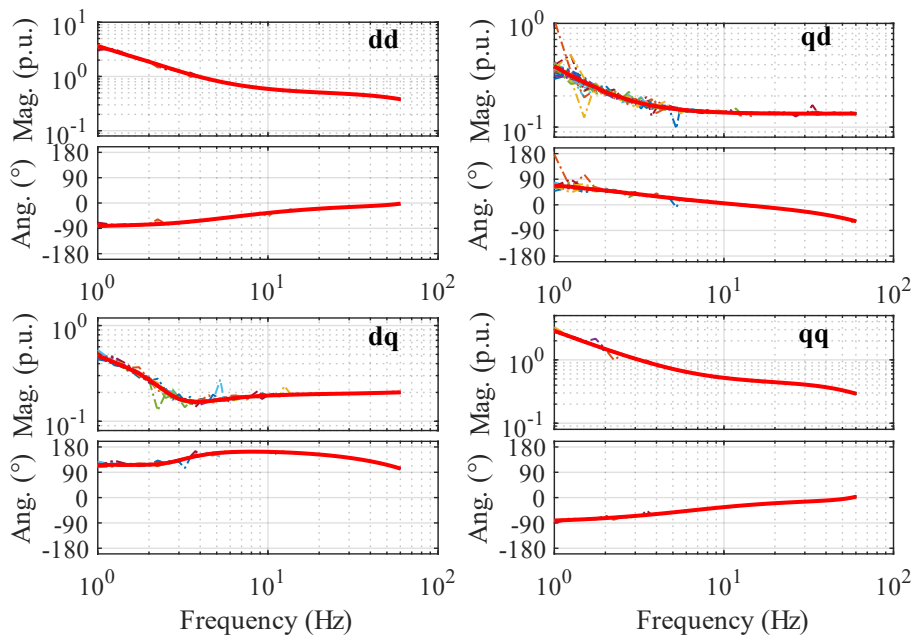


Figure 19 An overlay of one identified (thick red line) versus 200 predicted admittance (dot-dashed lines) of the black-box grid following inverter model at a randomly chosen OP.

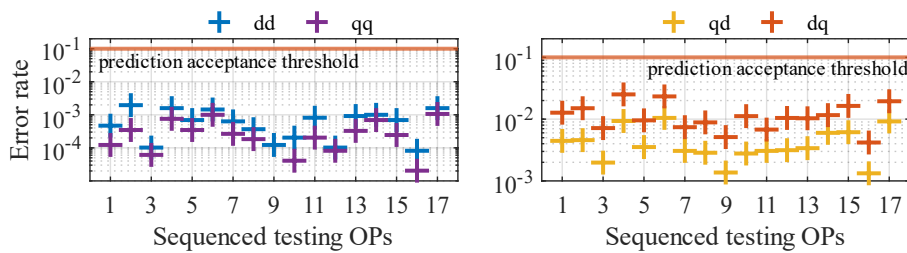


Figure 20 The mean error rate of the admittance prediction on 17 testing cases of the black-box grid following inverter model.

Grid-forming Inverter testing results

Figure 21 exemplifies the identified admittance versus 200 out of 1000 predicted ones of the black-box model, which was configured as a GFMI. In this case, the predicted admittances mostly overlay on the measured admittance, verifying the feasibility of (1) for the black-box model that was tested. Notably, dd- and qq-axis predictions have more inaccuracy than dq- and qd-axis predictions. The uncertainty mostly concentrates on the notch of qq-axis. Nonetheless, APM can be implemented on the given GFMI model as well. Further improvements need to be done to reduce uncertainties.

Figure 22 reflects the mean ratio of the wrongly predicted frequency-dependent admittance upon dd, qd, dq, qq elements in the predicted frequency range. The error rates of diagonal elements (dd, qq) are below 0.1 where qq ratio can exceed 0.1. The off-diagonal (dq, qd) error rates are below 0.001. As been seen previously, the errors concentrate around the qq- notch area. The low magnitude zone of impedance is rescanned with increased perturbation as an accuracy improvement measurement.

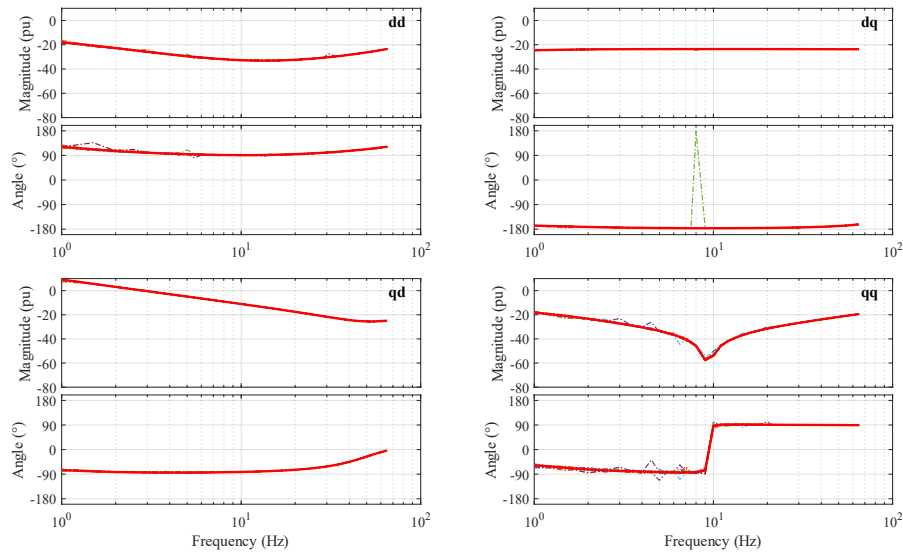


Figure 21 An overlay of one identified (thick red line) versus 200 predicted admittance (dot-dashed lines) of the black-box grid forming model at a randomly chosen OP.

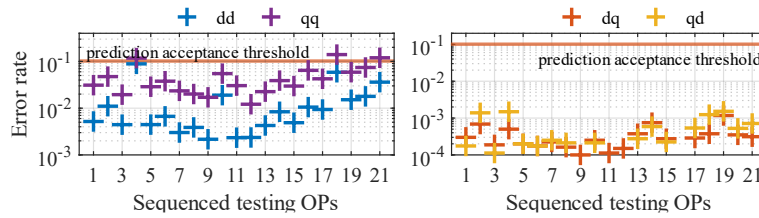


Figure 22 The mean error rate of the admittance prediction on 17 testing cases of the black-box grid forming inverter model.

5 A framework to analyse small signal stability of a network.

Recall in chapter 1 of this document, we mentioned that in order to assess the stability of power systems, when subjected to small perturbations, linear or small-signal analysis can be employed as an alternative to simulations. Linear methods allow efficient identification of underlying unstable dynamics and the participating equipment. However, the requirement for such analysis is the existence of a power system/ generation and load model.

As it is well-known, power system dynamics are non-linear in nature and thus any type of linear analysis requires linearization of dynamics around an operating point. These linearizations can be carried out either numerically or analytically and yield a representation that captures the stability properties of the system close to the operating point and when subject to small disturbances. These linearized models can be used for stability analysis via eigenvalue or frequency analysis, controller design and identification of groups of machines/ loads that participate in specific oscillatory modes. The final consideration when constructing and analysing such models, is the frequency of interest to be examined. System-wide studies have been conducted utilizing positive sequence models or RMS, i.e., models that assume balanced three phase operation, which usually neglect the frequency response of the power network's elements. When all the relevant circuit and high frequency dynamics are modelled, then the model is of the Electromagnetic Transient (EMT) type. In these types of models, phenomena like generator stator dynamics, detailed power electronic controls and filter and finally transmission network dynamics are fully incorporated. These models, as expected, are significantly more complicated, with multiple times more states than an RMS model.

5.1 Impact of EMT vs positive sequence admittance matrix

The initial step to examine the differences between EMT and positive sequence formulations is to examine fundamental examples used for small-signal analysis. For that purpose, the two examples utilized were based on the two-area Kundur System [9]. This system was introduced as a benchmark system to study and understand inter-area oscillations between groups of coherent machines.

For the study of the system, the following assumptions was considered:

- 1) Generators are modelled by sub-transient models
- 2) Generators are equipped with Exciter and PSS
- 3) Loads are modelled as constant admittance
- 4) Transformers are represented only by their leakage inductance

For the EMT cases, the network dynamics were fully modelled. Loads were assumed as shunt elements to ground and transmission lines represented by distributed T-sections, to capture the frequency response of longer lines more adequately. In the positive sequence setting, no network dynamics are assumed (algebraic representations) and lines are modelled by their Pi-section equivalent.

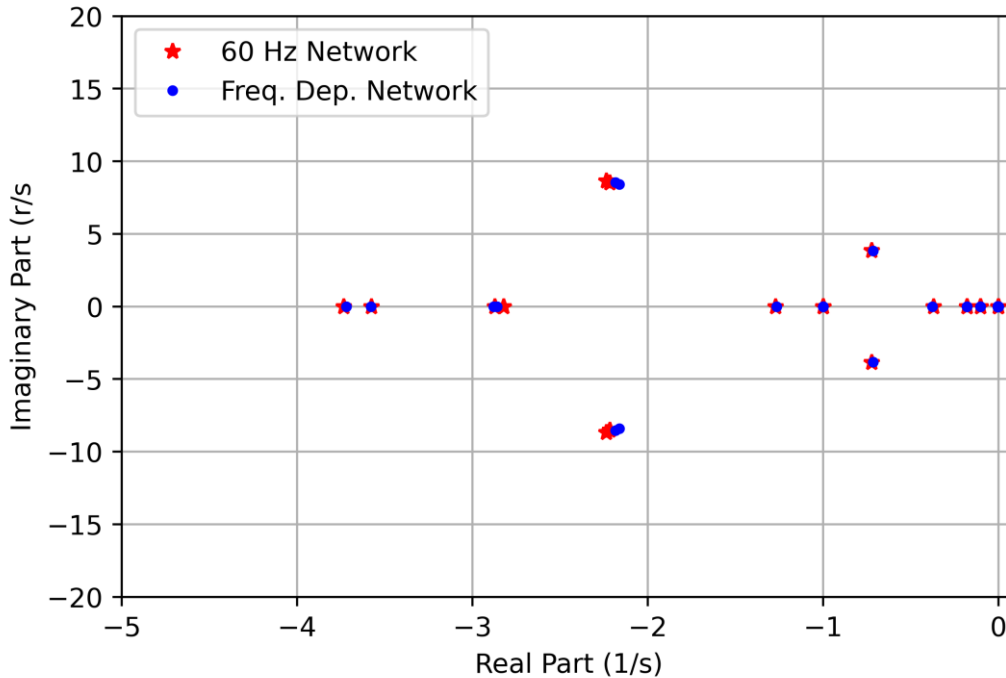


Figure 23 Two-Area System Eigenvalues in Complex Plain

In Fig. 23, the comparison of the frequency dependent network and the positive sequence 60 Hz equivalent are presented. Note, this test system uses a 60 Hz fundamental frequency. The frequency cannot be altered (to e.g. 50 Hz) without changing the dynamics, since it affects the rate of change of angles in the network, following a disturbance. While the actual value of the modes would change, the inferences obtained would not change since in a per-unitized setup, the effect on outcomes remains the same. In addition, since the power system stabilizers that have been tuned to damp the inter-area oscillation, given that the angle dynamics will be altered, might not offer the same phase required to achieve the same damping performance.

It should be noted that the modes in the lower frequency range depicted match adequately with small variations in the exact location of well damped modes around 7 r/s. The EMT formulation of the network yields higher frequency oscillatory modes, attributed to the RLC elements of the circuits. However, those modes remained well-damped. In addition, the inter-area mode between areas 1 and 2, appeared to not be affected by the network dynamics, as expected, given it occupies the frequency range of 0.6 Hz.

5.2 Incorporating non-linear loads

The next analysis conducted in the two-area system was to identify the sensitivity of the oscillatory modes in regard to load composition. For this study, the load composition from [9] was utilized, where active power loads are modelled as constant current, while reactive power loads are

modelled as constant impedance. When comparing the analysis' results with the results reported in the book very small deviations were observed.

Table 1 A comparison of modes for two area system incorporating non-linear loads between the small signal framework and reference values from [9] (in parenthesis)

CASE	MODE	FREQUENCY	DAMPING %
High gain Exciter	$+0.014 \pm 3.817j$	0.607 (0.61)	-0.4 (-0.8)
High gain Exciter + TGR	$+0.102 \pm 3.425j$	0.545 (0.55)	-3 (-3.6)
High gain Exciter + PSS	$-0.526 \pm 3.816j$	0.607 (0.60)	13.6 (13)

Compared to the constant admittance case, the damping of the inter-area mode, in the case where PSS was present in all machines, was worse.

5.3 Validation of small-signal stability framework

In the sequel, the team scaled up the small-signal analysis to the 39 Bus IEEE system [10], in order to establish the framework to efficiently import positive sequence model data and streamline the effort for the NEM network. In addition, this study served as an important benchmarking step for the methodology. As it can be noted from the step response comparison below, the response present quite similar frequencies, damping and shapes.

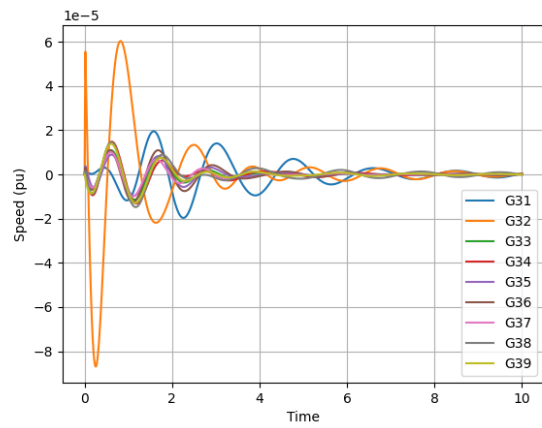
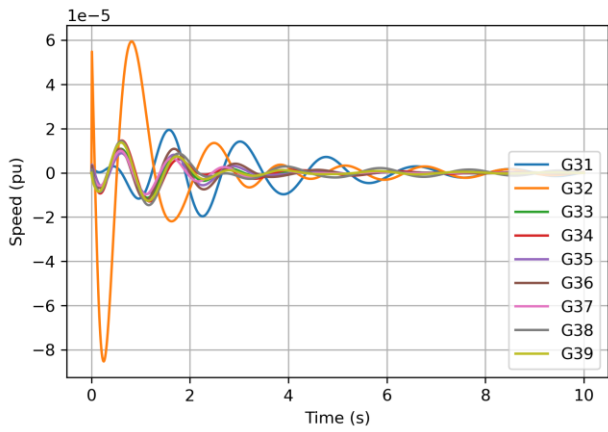


Figure 24 Impulse Response at Machine 32 Linearized Model (Left) Short High Impedance Fault Simulation (Right)

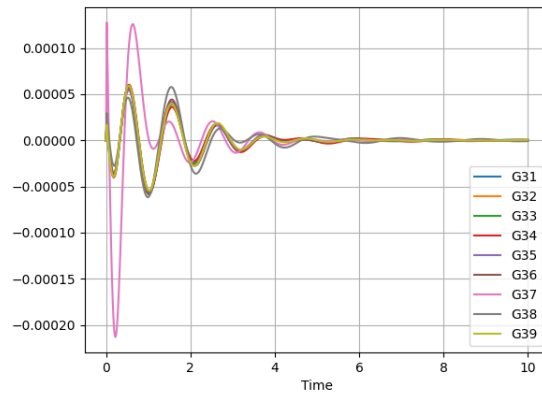
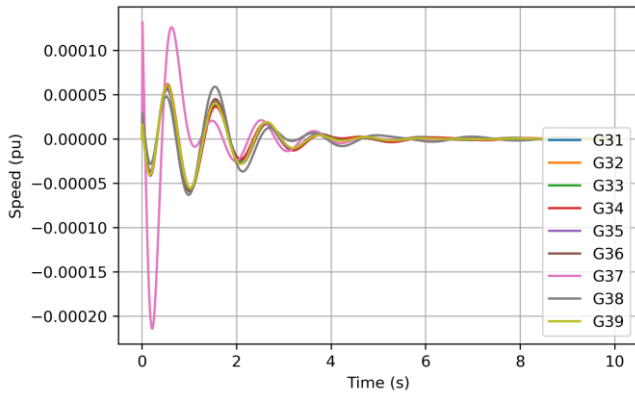


Figure 25 Impulse Response at Machine 37 Linearized Model (Left) Short High Impedance Fault Simulation (Right)

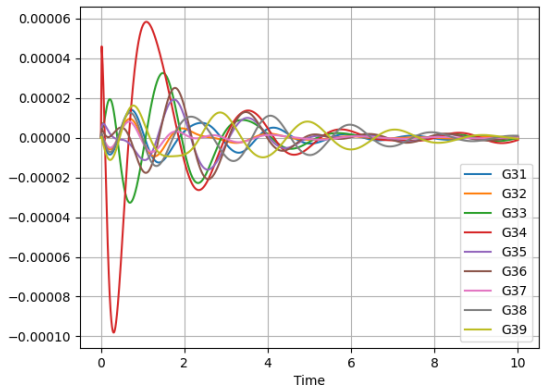
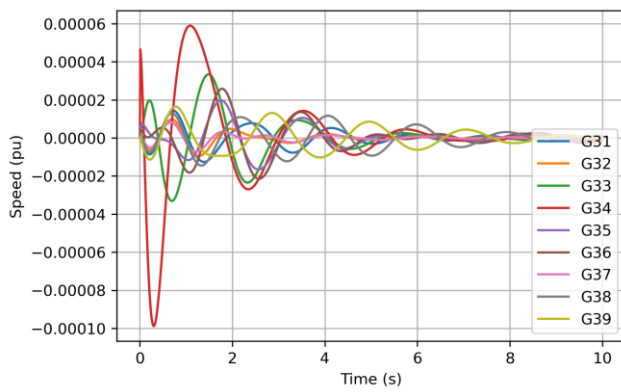


Figure 26 Impulse Response at Machine 34 Linearized Model (Left) Short High Impedance Fault Simulation (Right)

Eigenvalue analysis revealed multiple well damped oscillatory modes with multiple machines participating. Only one oscillatory mode was observed to be below 10% damping, with participation from generators 31-32-38-39.

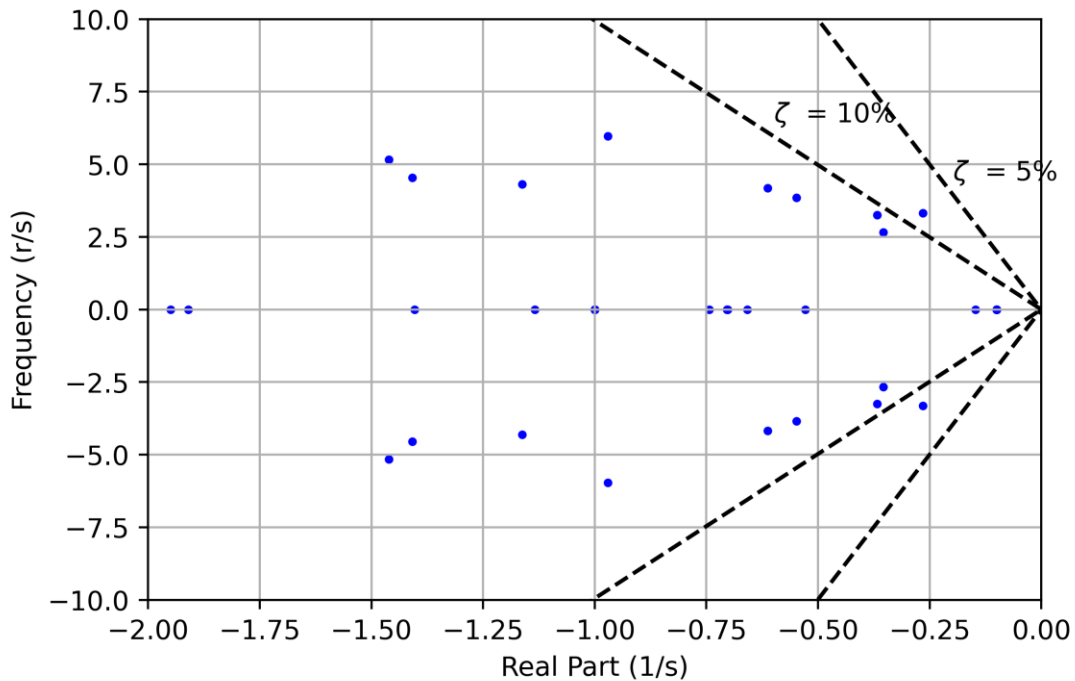


Figure 27 Eigenvalue Analysis of the IEEE 39 bus system

5.4 Incorporating IBR black box models in small signal analysis

In a small signal analysis framework, representing the different devices such as synchronous machines and IBRs in detail, modelling the control equations in detail is the norm. However, sometimes the control structure of the devices may not be fully known i.e., there might be black box models used/supplied for simulating a network. For such situations, the impedance or admittance characteristics of a device may be used to approximate how the device will interact with the rest of the network/devices for assessing small signal stability [2]. In this subsection, a procedure used to prepare such blackbox models for representing in a small signal framework is described. Such blackbox models can be software-based or hardware based (in case of a hardware, proper testing equipment/setup might be needed and there may be additional considerations).

The overall procedure to incorporate a model using its impedance/admittance frequency characteristics can be broken into several steps, as given below.

1. Obtain frequency scans for the IBR device at few select operating points
2. Use the obtained frequency scans as the training data for the IBR admittance estimation method(s) discussed previously in the report
3. From the network power flow solution, the required operating point(s) can be obtained where the device needs to be represented

4. Using the IBR admittance prediction algorithm, the IBR admittance frequency characteristics at the required operating points are estimated. These are in the format of the admittance or impedance values for a pre-determined set of frequencies.
5. A vector fit method is then used to fit a model representing the IBR characteristics. This can be in the form of a transfer function or a state space model.
6. The state space model thus formed can be incorporated into the network model by converting/transforming the inputs and outputs into the required frame of reference or format.

This subsection describes the application of this process for one of the black box models studied in Chapter 4. The details regarding the frequency scans conducted on the black box IBR model and application of the admittance prediction method to the blackbox model are presented in Chapter 4. However, there are certain nuances when applying the admittance characteristics thus obtained through the rest of the steps mentioned to integrate the models in the small signal analysis.

To start with, an analytical model of the blackbox IBR is created for validation purpose, and the impedance characteristics obtained from the frequency scan/admittance prediction method are compared with the frequency characteristics obtained from the analytical model. Figure 28 shows the magnitudes and phase angles of the four impedance terms compared for one of the IBR operating points. These operating points are chosen to be obtained from the synthetic NEM power flow solution. On the other hand, the training points for APM are chosen as a set of randomly determined operating points.

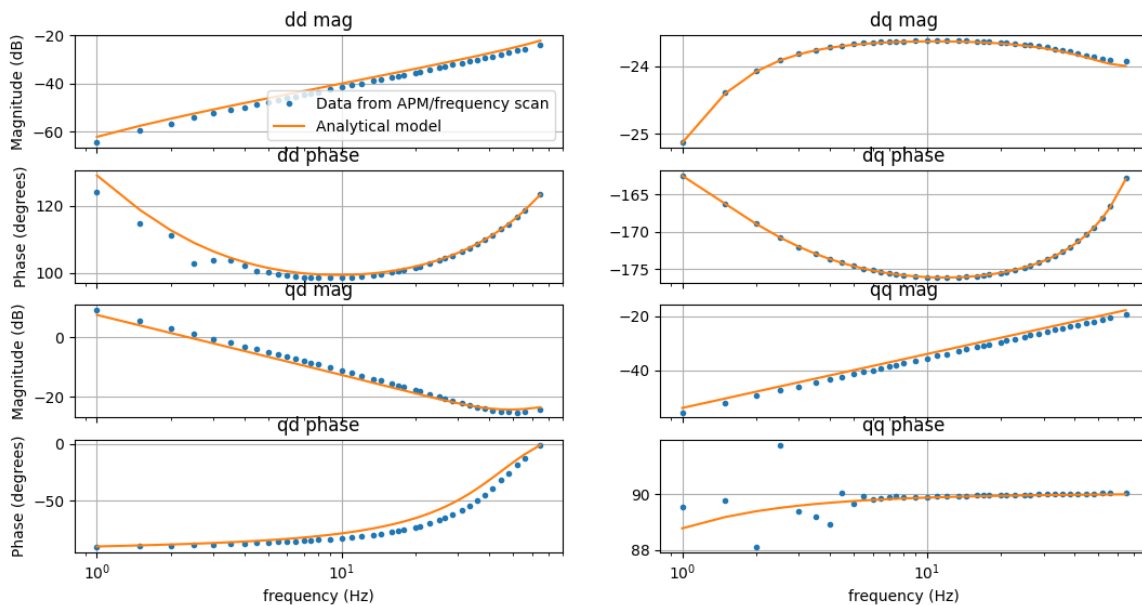


Figure 28 Comparison of the impedance characteristics obtained for the black box models for one of the IBRs against analytical small signal model

The frequency response from the analytical model and the predicted frequency are observed to match well for this blackbox model. Now, taking the frequency characteristics obtained from the frequency scan/admittance prediction method, vector fitting may be used to create an approximate model that exhibits the input-output frequency response very close to the

impedance or admittance characteristics obtained from the admittance prediction method and frequency scans. Here, a vector fitting package described in [14], [15] and [16] is used – different implementations of this package are available for MATLAB and Python languages. For this project, the MATLAB package is used. Given that the IBR device is represented in dq frame, the model has two inputs and two outputs corresponding to the currents and voltages in the dq frames. The vector fitting is performed together for terms with the same input. The two fitted state space models corresponding to two inputs thus generated are then combined to form a two input/two output model required to represent the entire device. This state space model with the IBR terminal currents and voltages as inputs/outputs can be incorporated with the rest of the network small signal model to include the selected device in the small signal analysis. For the same operating point as Figure 28, Figure 29 shows the frequency characteristics from the admittance prediction method/frequency scan (input data for the vector fitting) and the vector fitted model, showing that the vector fit is successful in reproducing the frequency characteristics captured in the input data.

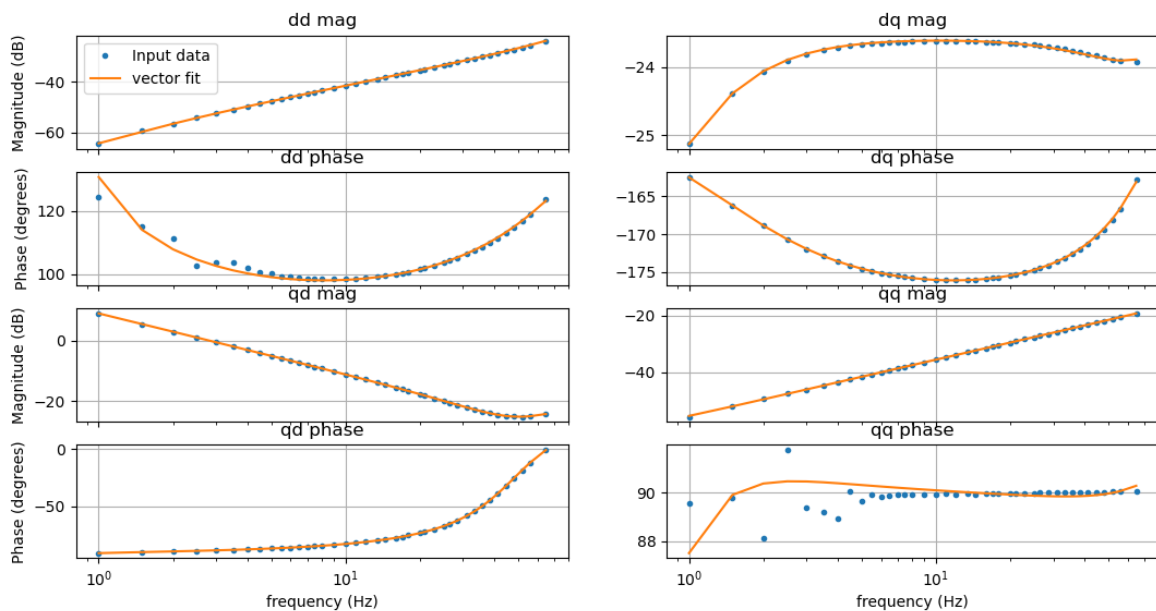


Figure 29 The input frequency data obtained from admittance prediction method/frequency scan compared with the vector fitted model for one IBR

However, there are certain nuances that are important to consider here. In Figure 28, the reference location selected for injecting the disturbance and measuring the IBR characteristics is at the terminal of the IBR, and the frequency characteristics observed from the frequency scan match the frequency characteristics obtained from the analytical small signal model of the IBR device. However, the reference location selected for the frequency scan/admittance prediction method is different (as explained in Subsection 4.2.2) for the IBR acting in the grid forming and grid following mode depending on the pre-requisite tests assuming no knowledge of the IBR control. It is observed that when the IBR frequency scan location is different, the frequency characteristics obtained from the frequency scan/admittance prediction method are different (Figure 30) to the analytical model that in both cases provides the small signal characteristics at the IBR terminal. This difference may indicate a need to standardize the IBR test procedures involving appropriate and consistent frequency scan procedures.

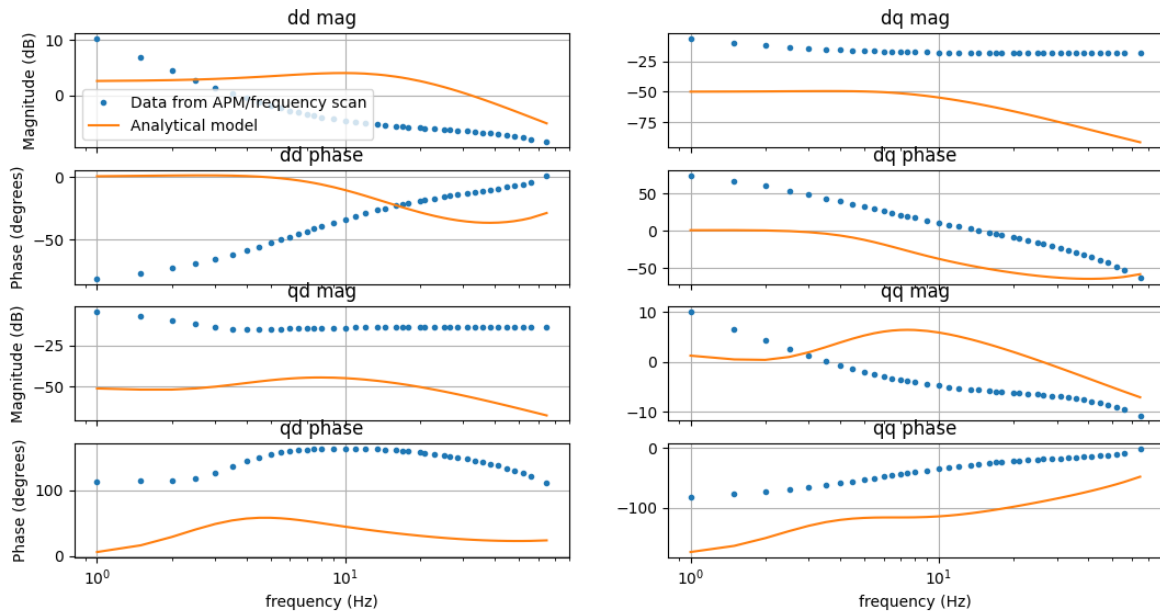


Figure 30 Comparison of the impedance characteristics obtained for the black box models for one of the IBRs against analytical small signal model - different scan reference location

Another aspect to consider here is the range of frequencies chosen for the frequency scan. While a good vector fit is observed for the GFM device in Figure 29, and thus the vector fitted model approximates the IBR device frequency response in this frequency range, the model may or may not match outside this frequency range. Here, for example, if the IBR device frequency response/characteristics from the analytical small signal model are compared with the fitted model based on the frequency scans (Figure 31), it is observed that the fitted model matches with the analytical model in the frequency range included for the fitting process, there are differences in the characteristics outside the range of frequencies covered by the frequency scans, both in the lower frequencies and in the higher frequencies.

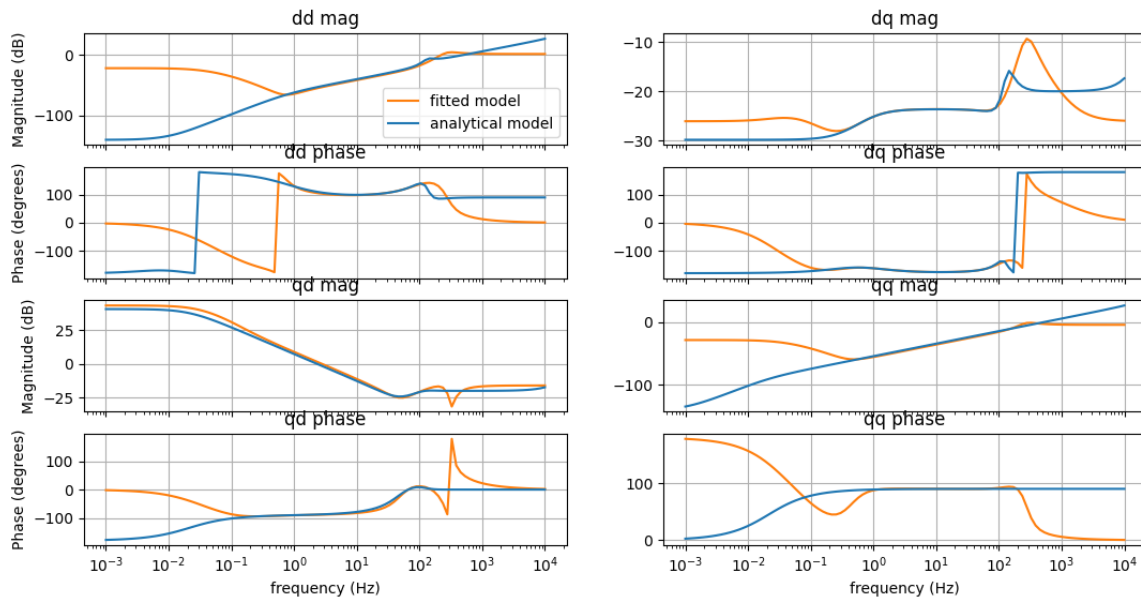


Figure 31 Vector fitted model based on the data from frequency scans/admittance prediction method compared with the analytical IBR small signal model, over a large frequency range

This points to the importance of selecting the frequencies to include in the frequency scan carefully so that the scan captures all poles and zeros of the model in the relevant range. Note that ‘relevant range’ may mean a wide frequency range or it may exclude some regions, but it might also depend on the analysis considered. For example, phasor-domain tools and analysis only consider lower frequencies of less than around 10 Hz, or a network operator may choose to focus on frequencies lower than the fundamental frequency or up to a 100/200 Hz that usually cover some of the slower IBR controls such as the phase locked loop or power controls for a particular study. In such case, representing the higher frequency characteristics accurately may not be as important. Two key challenges in the frequency selection/scan process are:

- Since the model under test is assumed to be a black box model, complete knowledge of all the poles and zeros of the system may not be possible, and more investigation and standardization of the range of frequencies to be considered might be required to ensure that the frequency scans capture the required IBR characteristics.
- As more frequencies are added to the list of frequencies the model is scanned at, the computational burden of each frequency scan also increases. This may be a particular issue if a large number of devices are to be studied in such a manner. When performing the frequency scan, it is important to capture several cycles of the disturbance injected at the selected frequency, hence, the frequency scan process is particularly time consuming for lower frequencies since they have longer time periods. For example, to capture 10 cycles of a 1 Hz disturbance, the model must be simulated for at least 10s, while for the 0.01 Hz disturbance, simulating the model for 1000s is required to capture 10 cycles. This can be challenging for very detailed models demanding more computational resources for simulation.

Considering these practical challenges and differences, for illustrating how blackbox IBR models may be represented in a large network model, in Section 6.3, the frequency scans obtained from

the analytical small signal models are used instead, including IBR characteristics at the frequencies used in the frequency scans described in Chapter 4, but also including lower frequencies up to 0.01 Hz to sufficiently capture the lower frequency characteristics of the IBR device under consideration.

6 Small signal stability of synthetic NEM network with IBRs

A synthetic network model representing the NEM footprint was selected to test the small signal stability framework used in this project on a larger circuit. This system originally had ~2300 buses and ~256 generators. The network model from [5] was used in the last stage of the project for creating the test cases, and more details regarding the development of original synthetic NEM network and work based on the synthetic NEM network can be found through multiple references such as [17], [18], and [19]. The synthetic network is plotted to illustrate the different NEM network regions in Figure 32. The figure also shows the locations of IBRs considered in this project.

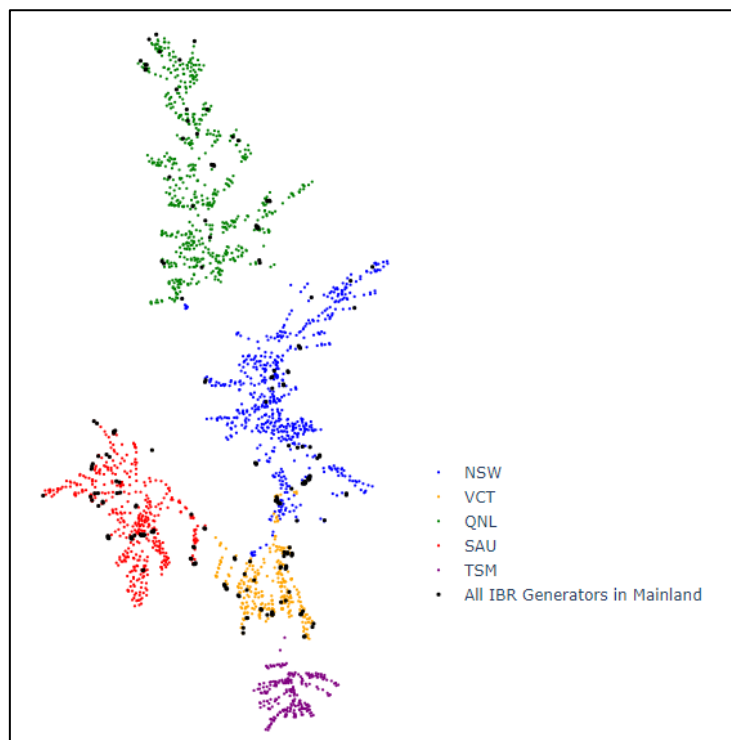


Figure 32 An approximate representation of the synthetic NEM network on the map of Australia

6.1 Operating point and data selection

From the 24 hourly cases created in the previous stage, the peak load case (hour=19) was selected as the initial operating point for studying the NEM network. In the preliminary dynamic simulations conducted for this case in the previous stage of the project, it was shown that for a network disturbance of tripping a load (~20 MW), the synthetic NEM modelled exhibited oscillations/small signal unstable behaviour when all IBRs were set to be grid following, as shown in Figure 33. However, adding just 35 IBRs with grid forming controls (to existing 199 IBRs with grid following controls), the oscillations were damped.

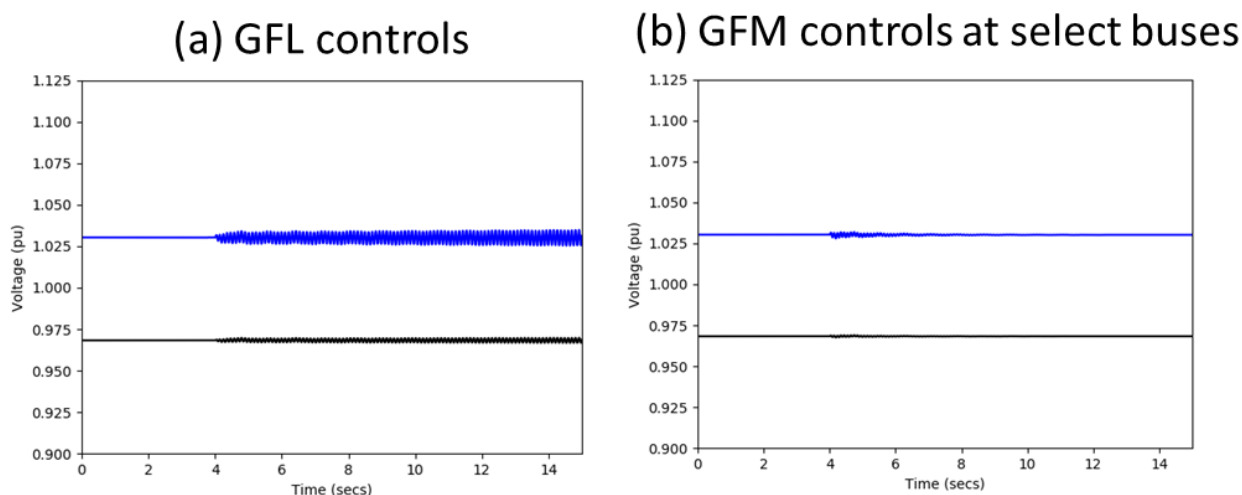


Figure 33 Time domain simulation results for a load trip - (a) when all IBRs have GFL controls and (b) when a select number of IBRs have GFM controls for the selected peak load (hour=19) operating point

Hence, this operating point was selected for testing the small signal model on the system. Table 2 provides some key powerflow details for the selected operating point. Note. Since Tasmania Island area is reduced to a single generator, it is not shown in Table 2.

Table 2 The load, generation and interarea flows in different areas of the synthetic NEM network for the selected operating point

AREA	LOAD (GW)	GENERATION (GW)	INTERAREA FLOW (MW)			
			TO NSW	TO VCT	TO QNL	TO SAU
NSW	10.220	9.607		-16	-901	
VCT	6.424	6.048	16			-516
QNL	6.424	7.559	901			
SAU	1.070	1.670		516		
Total	24.139	24.886				

6.2 Analysis with white box IBR models - GFLs/GFMs

This section will present the linear or “small signal” analysis of the synthetic NEM system for hour 19. For the purposes of this investigation, we will initially highlight all the assumptions made for the model:

- 1) Synchronous generators are represented by the GENROU type model with frequency dependence of the terminal voltage/ flux.
- 2) Loads can be either of the constant current or constant admittance type for active power and constant admittance for reactive power.
- 3) GFL IBRs are represented by the REEC_C model for electrical controls and REGC_C for the converter controls.
- 4) GFM models are represented by EPRI’s generic GFM model.

- 5) The network and loads are modelled in their 50 Hz constant representation without any frequency dependence.

Case 1

For this case, we are assuming the existence of only GFL IBRs in the system and constant current active power loads. The simulated step response of the entire linearized synthetic NEM system for a disturbance at the terminals of generator 5, can be noted below:

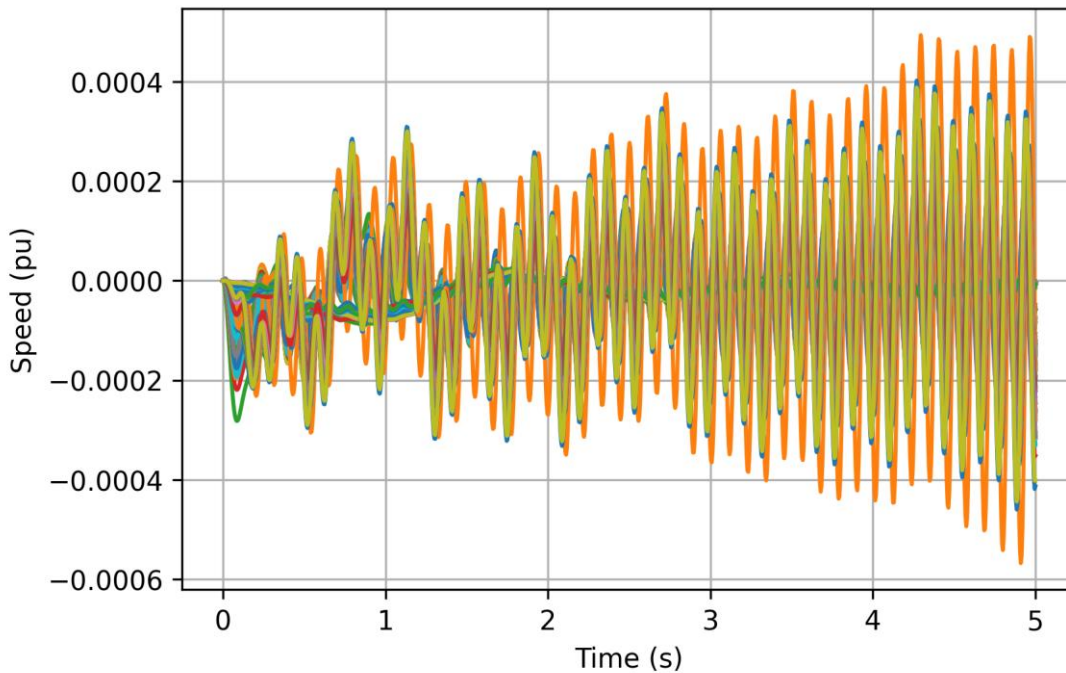


Figure 34 Linearized System SG-GFL IBR Speeds Impulse Response (for IBRs Speed is the PLL integrator state)

As it can be seen, the system presents a fast unstable mode, previously identified in time domain simulations. Upon inspection of the eigenvalues, the mode has been identified to have a frequency of 8.929 Hz with a damping ratio of -0.4%

Upon further examining the participation factors of the mode, the following generators appear to present significant participation (above 0.1 absolute value when normalized to the maximum element of the participation factor) in the unstable mode:

Synchronous Generators:

731, 730, 732

IBRs:

5, 6, 18, 19, 20, 21, 31, 34, 35, 36, 37, 38, 39, 40, 41, 42, 43, 56, 64, 65, 66, 67, 69, 70, 73, 74, 75, 647, 648, 654, 655, 658, 659, 660, 665, 668, 672, 674, 680, 681, 682, 684, 685, 687, 688, 689, 690, 691, 693, 694, 695, 696, 697, 698, 699, 700, 701, 702, 703, 712, 721, 728, 729, 733, 956, 986, 1636, 1640, 1641, 1646, 1651, 1652, 1653, 1654, 1655, 1656, 1658, 1659, 1660, 1661, 1662, 1663, 1665, 1666, 1667, 1668, 1679, 1681, 1682, 1683, 1684, 1685, 1686, 1690, 1691, 1692, 1693, 1694, 1695, 1696, 1697, 1699, 1705, 1706, 1708, 1709, 1710, 1711, 1715, 1716, 1719, 1720

As it is evident, the mode appears to present participation from machines across the NEM system. When inspecting the list of IBRs with negative available MVA found in Stage 2, we can note that there exists a significant overlap (Table 3).

Table 3 IBR buses with lowest available MVA identified in the previous stage of the project, and the participation factors of these IBRs in the unstable mode

Bus	MVA Available	Normalized to Max PF
1663	-929.680824	1
1693	-409.63707	0.9
1694	-407.433033	0.92
1685	-401.246548	0.67
1695	-397.394753	0.47
1684	-368.928051	0.68
1686	-358.293247	0.7
689	-242.50145	0.79
655	-180.611277	0.33
986	-165.426064	0.93

When examining the buses with the lowest available MVA, we can note that there is a correlation between low SC capability and participation in the instability, i.e., propensity to instability. The participation factors of the unstable mode were normalized against the maximum to make it easier to compare values. The plant with the most MVA deficit appeared in the participating states, indicating that MVA available can be a good metric to screen the potential instability of IBRs.

In terms of which states, appear to participate, the most impactful states were comprised by the VSC voltage states (which is to be expected given the high frequency instability). Other states that participated are PLL angles of some IBRs, the voltage transducer state of the REEC_C controller (s0) and finally, the voltage regulator state (s3). Aside from the fast IBR driven unstable mode, there exist other angle dynamics in the linearized system. In particular, there exist multiple rotor angle modes with frequencies below 2 Hz. Several present damping below 10% with the least damped having a damping ratio of 0.5%. This particular mode presents participations from generators at buses 3, 4, 76, 77, 730, 731 and 732.

Case 2

As a countermeasure to these high frequency instabilities, and the weak state of the grid, droop-based GFM IBRs were installed on the buses with low available MVA values. Those GFMs do not contribute any pre-disturbance power but are installed to stabilize the grid. As it can be noted in the updated step response, the 9 Hz unstable mode stabilizes.

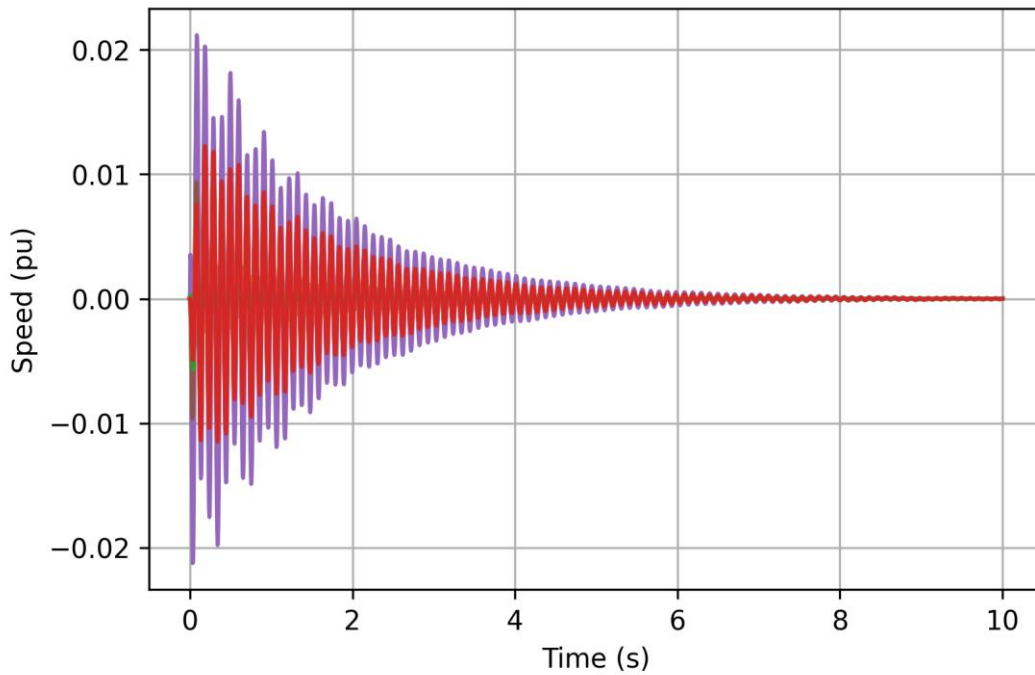


Figure 35 Linearized System SG-IBR Speeds Impulse Response

The marginally stable mode occupies the frequency of 9.663 Hz with a damping ratio of 1%. Lower frequency dynamics are still visible, but they appear well-damped. In the sub 2 Hz range, the previously low damping mode presents an increased damping ratio of 2.5%. The marginally stable high frequency modes still present participation by mostly GFL IBR states and not the GFM plants.

6.3 Impact of Load Modelling

To examine the impact of load modelling on the stability of the system, the case where both active and reactive power load are represented as constant impedance is examined. In Case 1, where all IBRs are GFL, the 9 Hz mode is no longer unstable. Now the instability occurs at lower frequencies, and particular at 1.1 Hz.

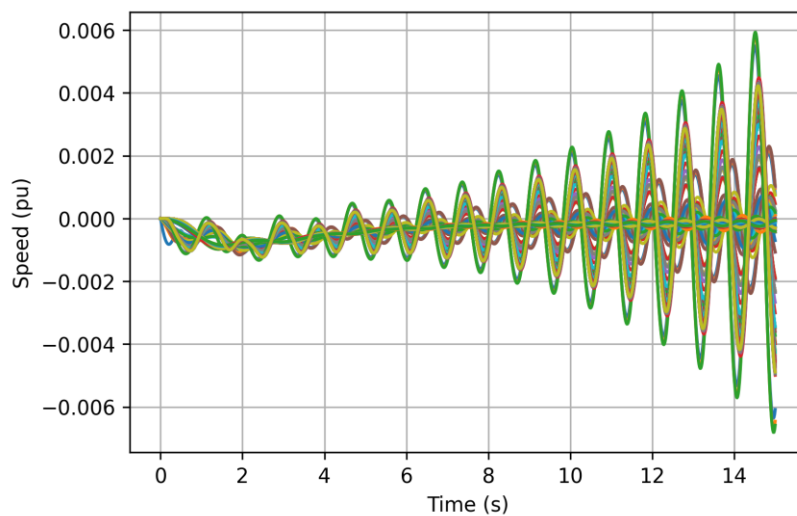


Figure 36 Linearized System SG-IBR Speeds Impulse Response with all loads represented as constant impedance

In this mode, participation is observed from the following generators.

Synchronous Generators:

3,4,76,77,730,731,732

IBRs:

684,685,687,688,689,690,691,702,703,712,728,730,731,732,733

The synchronous generators mostly present participation from the rotor mechanical states. The IBRs present significant participation from the PLL states and the voltage control state.

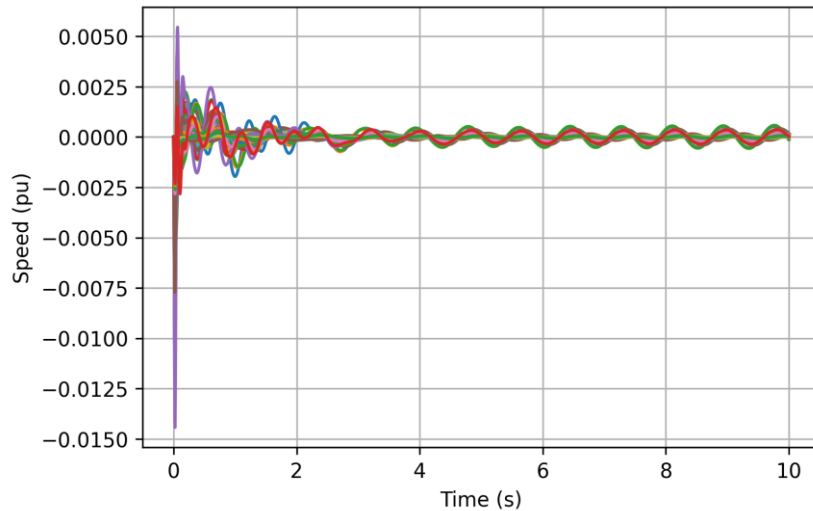


Figure 37 Linearized System SG-IBR Speeds Impulse Response with GFM Plants

Inclusion of GFM plants, improves the damping of the unstable mode but fails to stabilize it. The mode now has a damping ratio of -0.5 %. As this instability appears to be rotor angle driven, given the participation of synchronous generation and the lower frequency, GFM plants appear to aid slightly but given they are modelled as droop-based, they do not yield such significant impact in the lower frequency ranges, due to absence of virtual inertia of the power synchronization loop.

6.4 Figure 38 NEM Network Simulation with Constant Admittance Loads Incorporating blackbox IBR models in the network analysis

Once the synthetic NEM network is demonstrated with the white box IBR models, this subsection demonstrates how the blackbox IBR models are prepared to be incorporated into the network small-signal analysis. The overall procedure followed is described in previously in Section 5.4, here the details more pertinent to the actual network considered and the models considered are provided.

As mentioned at the end of Section 5.4, the frequency scans used here are obtained from the small signal analytical model. The list of frequencies chosen for obtaining the frequency scans include the frequencies considered in Chapter 4 as well as 20 more frequencies in the lower frequency range from 0.01 Hz to 1 Hz in addition to capture the lower frequencies. Throughout the process, the analytical small signal model of the IBR is used for validating the developed procedure to create the small signal models.

For this case study, the 35 newly added grid forming IBRs are considered to be replaced/represented using blackbox models. Hence, the active power, reactive power and

voltage magnitude for these 35 models are extracted from the network power flow solution. At these operating points, the frequency characteristics are obtained using the admittance prediction method by considering 39 operating points, randomly chosen, as training points for the method, These training points are chosen randomly from the region encompassing the maximum and minimum values of voltage, reactive power and active power from the 35 operating points for more accurate prediction. With such a training dataset, the admittance prediction method successfully approximates the IBR frequency characteristics at the 35 operating points – for one of the operating points the impedance predicted is compared with the impedance from the analytical small signal model as validation in Figure 39.

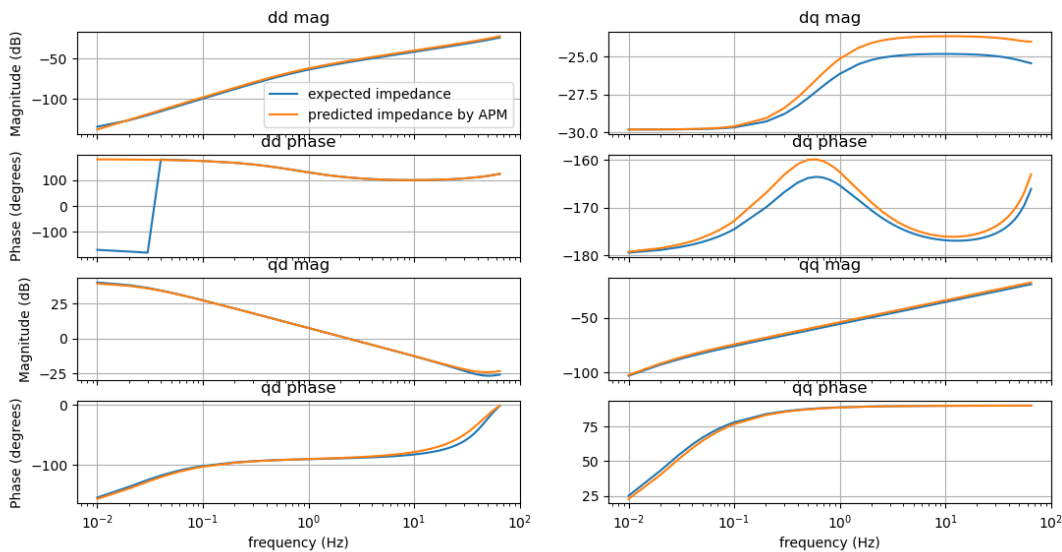


Figure 39 Expected versus predicted impedance based on admittance prediction method

Vector fitting is then applied to the predicted impedances corresponding to the 35 operating point – terms corresponding to d-axis input are fitted together, and terms corresponding to q-axis input are fitted together. Note, one of the impedance terms (Z_{qd}) requires a pole with a positive real value for obtaining a good fit (as illustrated in Figure 40), hence such poles are allowed while fitting the terms with d-axis inputs, while stable fitting is ensured when fitting the terms with q-axis inputs. Note, since open-loop frequency response of the IBR device is fitted, there may be some eigenvalues/poles with positive real values, however, once the IBR is connected to a network such that the IBR operate stably, such eigenvalues can be expected to move to negative real plane. The vector fitted model is compared with the input data used (the predicted impedances at different frequencies), as shown in Figure 41.

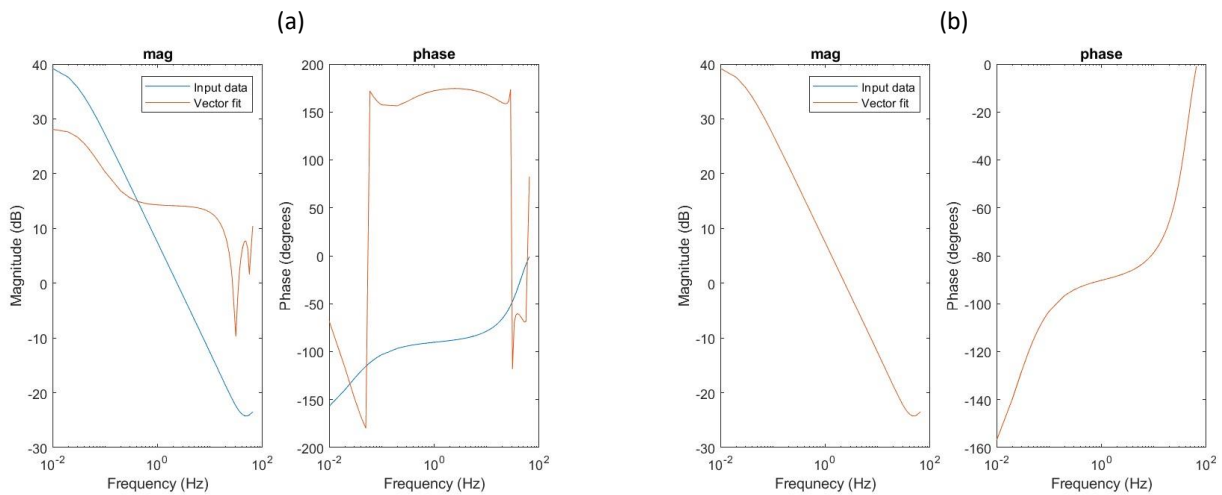


Figure 40 Vector fitting the qd term without allowing a pole with positive real value (a) and allowing a positive real value (b)

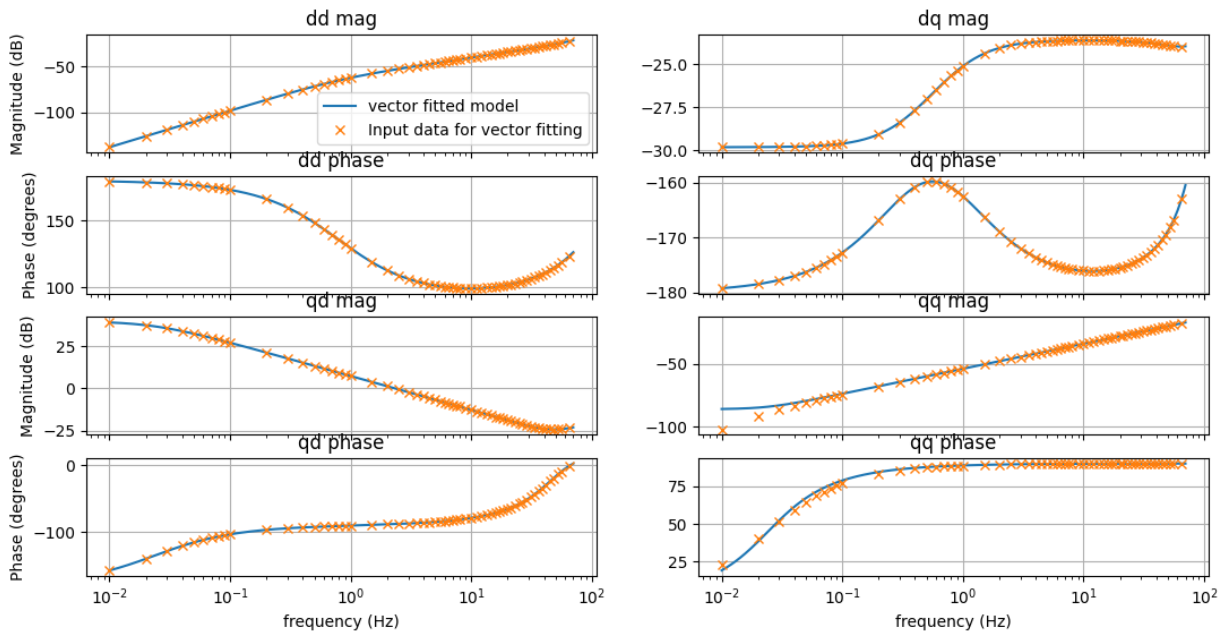


Figure 41 Vector fitted model compared with the input frequency characteristics for an IBR model

Once the vector fit is successful, the models for the d-axis input and q-axis input are combined to form a single two input/two output model. For each of the 35 operating points, the frequency response from the fitted models are compared with the analytical models for validation over a larger range of frequencies, for one of the IBR models this comparison is shown in Figure 42. Notice, there are some mismatches in the higher frequencies outside of the frequency range considered for the frequency scan. For the considered analysis, this higher frequency range is not a focus. A mismatch is also observed in the lower frequency range outside the frequency range used for the frequency scan. This mismatch/difference between the analytical and fitted models is relatively small (below 10^{-5} p.u.).

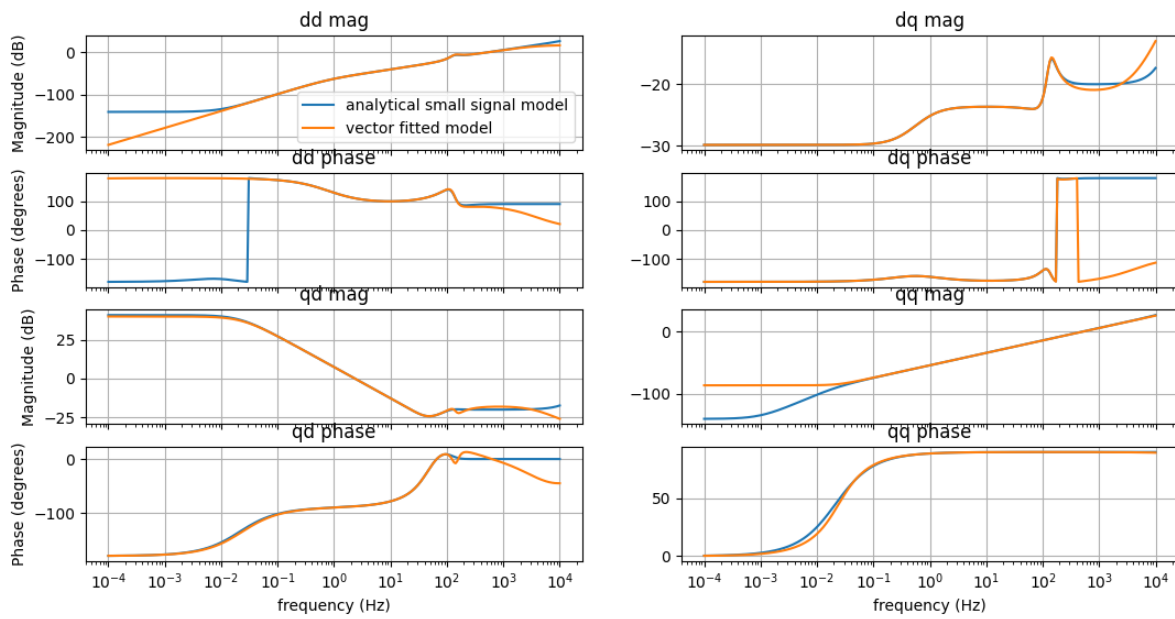


Figure 42 The frequency response of the vector fitted model compared with the analytical small signal model over a wide range of frequencies

As a further validation, the closed loop poles of the analytical and fitted models are compared in Figure 43 for one of the IBRs. It is observed that while the fitted model does not capture all the poles of the analytical model, it closely approximates several poles of the analytical small signal model.

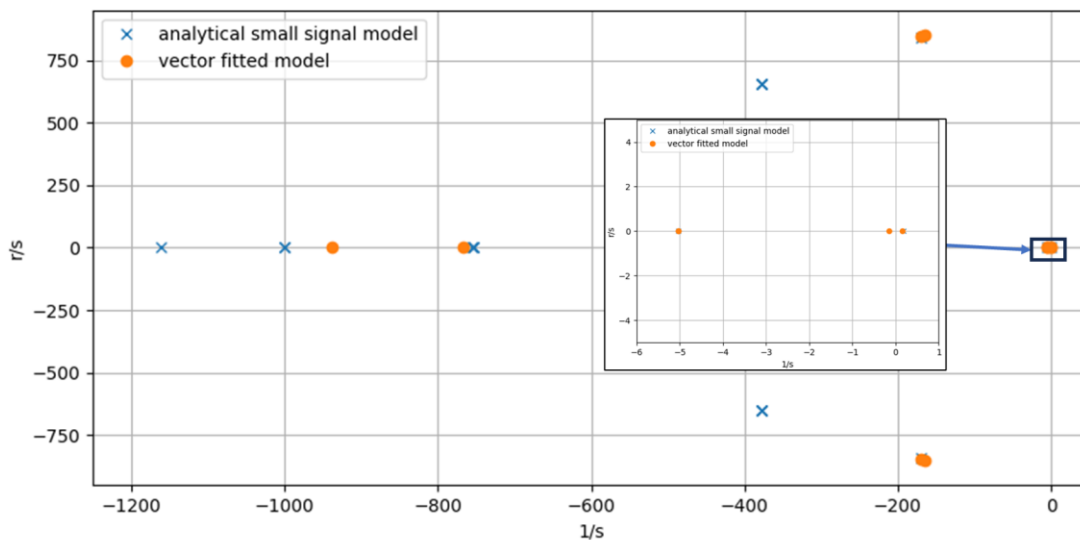


Figure 43 A comparison of the poles of the open loop fitted model of the IBR and the open loop small signal analytical model of the IBR

Additionally, the fitted models are validated using a single machine infinite bus-type test network. At the required operating point, the impedance of the infinite bus is gradually increased (SCR is decreased) and the value of SCR at which the model shows small signal unstable behaviour is compared between the fitted and analytical model as a validation. It is found that the fitted model exhibits similar values of SCR at which it goes unstable, as denoted in Table 4. Here, the SCR value

is calculated assuming a maximum active power of 1 p.u. is possible. Note that since this is a grid forming type model expected to perform well in weaker (low SCR) situations, the SCR values at which an unstable pole is observed are low. The black box time domain model is also observed to remain stable under very low SCR values.

Table 4 A comparison of the fitted and analytical models in terms of the SCR value exhibiting unstable behavior

Bus Number	P (p.u.)	Q (p.u.)	V (p.u.)	SCR at which a positive real pole is observed	
				Analytical Model	Fitted Model
2348	0	0.009468	0.9686	0.01	0.01
2350	0	0.003445	0.9679	0.003	0.003
2352	0	0.003548	0.9667	0.003	0.003
2354	0	0.024142	1.0398	0.02	0.02
2356	0	0.022783	1.0395	0.02	0.02
2358	0	0.037724	1.0395	0.03	0.03
2360	0	0.013566	1.0394	0.01	0.01
2362	0	0.012506	1.0716	0.01	0.01
2364	0	0.001783	1.0679	0.001	0.001
2366	0	0.002555	1.0014	0.002	0.002
2368	0	0.001252	1.0018	0.001	0.001
2370	0	0.013732	1.0832	0.01	0.01
2372	0	0.005749	1.0091	0.005	0.005
2374	0	0.019102	1.0178	0.01	0.01
2376	0	0.001778	0.9775	0.001	0.001
2378	0	0.003974	0.9936	0.004	0.004
2380	0	0.065185	0.9039	0.08	0.08
2382	0	0.013266	1.0118	0.01	0.01
2384	0	0.003238	1.0007	0.003	0.003
2386	0	0.000335	1.0168	0.001	0.001
2388	0	0.002369	1.1015	0.001	0.001
2390	0	0.000803	0.9725	0.001	0.001
2392	0	0.000739	0.9722	0.001	0.001
2394	0	0.000827	0.9725	0.001	0.001
2396	0	0.0029	0.9677	0.003	0.003
2398	0	0.003198	0.9683	0.003	0.003
2400	0	0.002864	0.9674	0.003	0.003
2402	0	0.000728	0.9782	0.001	0.001
2404	0	0.000732	0.9781	0.001	0.001
2406	0	0.00075	0.9778	0.001	0.001
2408	0	0.001956	1.0065	0.001	0.001
2410	0	0.002352	1.0283	0.002	0.002
2412	0	0.025528	1.0132	0.02	0.02
2414	0	0.002658	1.012	0.002	0.002
2416	0	0.027693	1.0189	0.02	0.02

Finally, we integrate the identified dq impedance models with the rest of the linearized power system and perform small-signal analysis on the closed-loop dynamics.

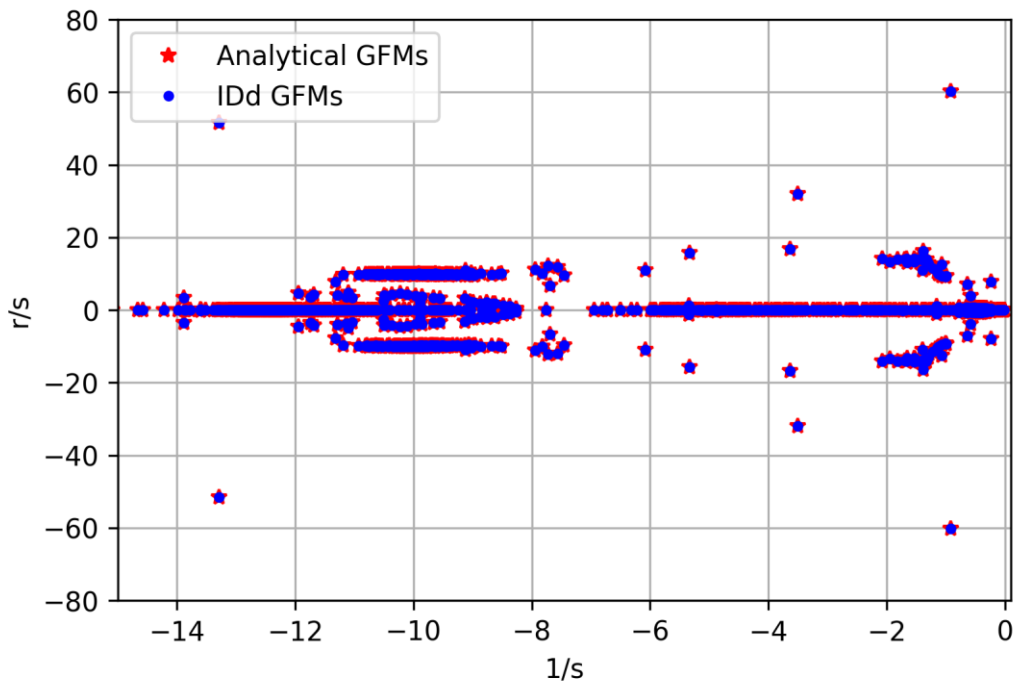


Figure 44 Closed Loop Poles of System with Analytical and Identified Models

As it can be noted, if the models are sufficiently well estimated, the pole locations in specific ranges of interest can be approximated with great accuracy. In this case, the depicted pole locations appear to be matched exactly. Given that the examined GFM model is of the EMT type, the ranges of interest we can analyse should be at the lower frequencies (typically sub 10-15 Hz) since the frequency dependence of the network can start taking effect after that. The exact frequency range where EMT models are required to capture the correct small-signal behaviour of the system is an active field of research. At higher frequencies, even if the closed loop dynamics present some type of instability, the validity of this instability cannot be verified unless the complete frequency dependence of the network is properly represented.

6.5 Conclusions

In this chapter, the small-signal analysis of the synthetic NEM system was presented. In the original analysis of the peak loading condition, high frequency unstable oscillations were identified in linear and time-domain analysis. It was found via participation factor analysis that the GFL IBRs were major contributors to the instability. As a remedy, GFM plants were installed on the buses of the system where low SC conditions were identified and analysis was performed again. The installation of the GFM plants appeared to resolve the instability, improving its damping.

The second step was to examine the dependency of the identified stability issues on load modelling. For that purpose, the active power component, which was initially modelled as constant current, was recasted as constant impedance and the analysis was repeated. In that case, no high frequency stability issues were observed and the mode of interest occupied the low frequency range, with major participation from synchronous generation. Installation of GFM generation did not appear to aid significantly that mode, as most of the effects of a droop-based GFM, without any virtual inertia, appeared to be mostly realized in the higher frequency range (as

noted in the original case). Small-signal issues in the 1 Hz range can be addressed with proper power system stabilizer design or power oscillation dampers.

Finally, the integration of identified black-box models into the small-signal analysis framework was examined. For that purpose, the GFM plant analytical models were replaced by impedance models, identified via simulated measurements across a frequency range of interest. It was demonstrated that if the models' dynamics are adequately captured from the impedance scans and then fitted into a state-space representations, the dynamic behaviour of the closed-loop system can be correctly recovered. Thus, a hurdle in the use of state-space methods from linear analysis of power systems, it being models without any access to their internal control structure aside from terminal measurements, can be overcome via system identification and appropriate interface with the rest of the network.

7 Impact of current limits on IBR admittance characteristics

An IBR is a current limited device and as a result, stability at its pre-disturbance steady state operating point can be influenced by the maximum value of current that can be delivered. In a synchronous machine, this impact is lower because even if the machine operates near its power limit, there is sufficient over current capability that is available. However, in an IBR, due to the lower values of over current capability, operation at or near the power limit can be detrimental to the overall stability. Due to non-linear nature of limits the admittance characteristics of the IBR may change when limits become binding. One issue which arises when doing small signal analysis is that the non-linear elements, such as a limiter, cannot be represented. So, the question arises that what will happen if the IBR is working near to its current limits, how the eigenvalues, subsequently the small signal behaviour of the system will change? Let us assume that a PI controller is used to generate a signal u_d as shown below:-

$$u_d = \left(k_p + \frac{k_i}{s} \right) (x_d^{ref} - x_d) \quad (5)$$

Where, x_d^{ref} reference signal, x_d is the measured value of variable x . One way to represent (5) in small signal form is:

$$k_p (\Delta x_d^{ref} - \Delta x_d) = \Delta u_d - k_i (\Delta x_d^{ref} - \Delta x_d) \quad (6)$$

Let's say the variable x_d^{ref} is at its limit, because of this no further change in x_d^{ref} is possible. (6) will then be modified into:

$$-k_p \Delta x_d = \Delta u_d - k_i \Delta x_d \quad (7)$$

This shows that there will be a change to the A matrix of the system, which implies that it can also impact the eigenvalues. How significant will be the impact of this can be answered only by carrying out a detailed small signal analysis. We studied the impact of IBR current limits on small signal system stability using two area Kundur system shown in Figure 45 for cases shown in Table 5.

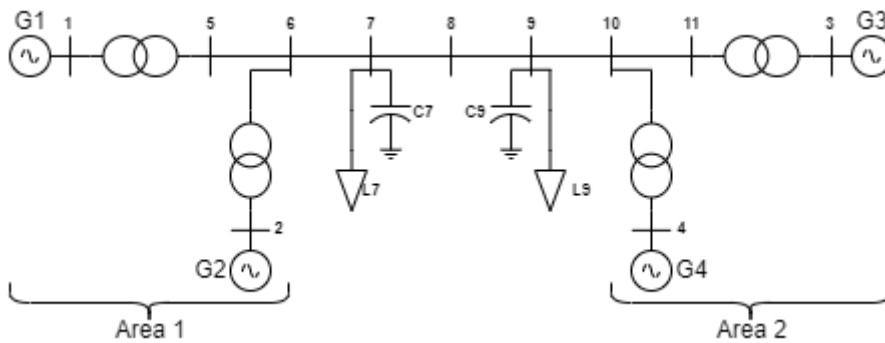


Figure 45: Single line Diagram of Kundur's Two Area System [9].

Table 5: Cases studied.

	Area 1	Area 2
Case 1	1 IBR	0 IBR
Case 2	0 IBR	1 IBR
Case 3	1 IBR	1 IBR
Case 4	2 IBRs	0 IBR
Case 5	0 IBR	2 IBRs

Case 1:

For this case SG 2 is replaced with a GFL IBR in Area 1; for our study we did not find any difference in the analysis based on the location of IBR (i.e. either G1 or G2 can be replaced with GFL IBR and the conclusion remains same). Figure 46 shows the eigenvalues that are closer to the imaginary axis and thus have higher impact on the system stability.

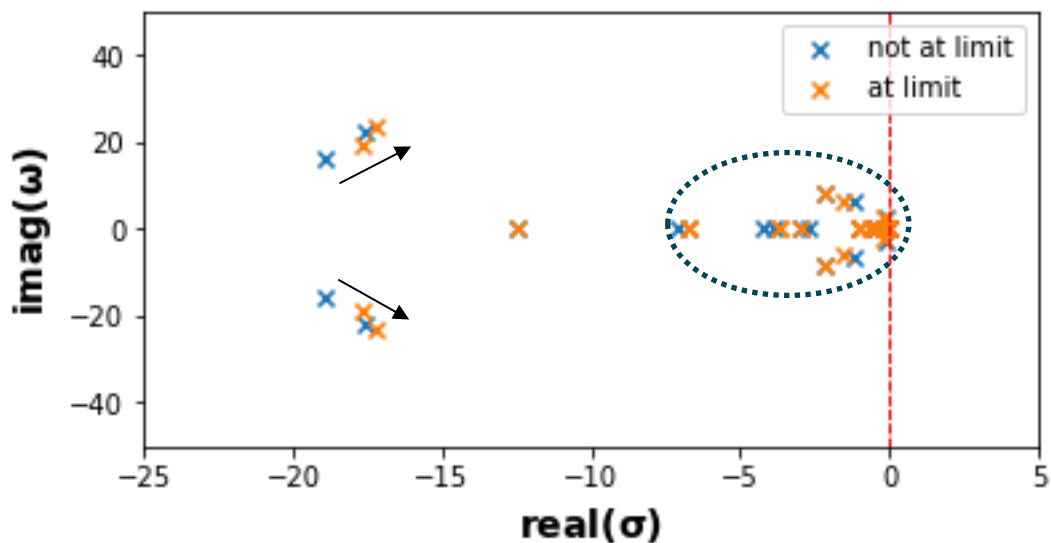


Figure 46: Eigenvalues for Case 1.

Figure 46 shows that when the GFL IBR is working at its current limit, then the eigenvalues with a slightly higher frequency component move slightly towards the imaginary axis.

Table 6: Eigenvalues when IBR is not operating at its current limit.

Eigenvalues	Damping ratio	Frequency (Hz)
-17.603±22.007j	0.625	3.503
-18.912±15.889j	0.766	2.529

Table 7: Eigenvalues when IBR is operating at its current limit.

Eigenvalues	Damping ratio	Frequency (Hz)
-17.651±18.935j	0.682	3.014
-17.184±23.277j	0.594	3.705

None of these eigen values are affected by the states of the GFL IBR when the IBR unit is working at its current limit.

Figure 47 shows the eigenvalues in the circled region of Figure 46 . Eigenvalues of particular interest are marked by region 1, and 2.

Region 1 being closer to the imaginary axis is more likely to cause small signal instability. Table 8 shows the eigenvalues of region 1 and 2 when IBR is not working at its limit.

Table 8: Eigenvalues of region 1 and 2

Eigenvalues	Damping ratio	Frequency (Hz)
-0.109±2.641j	0.041	0.42
-1.167±6.446j	0.178	1.026

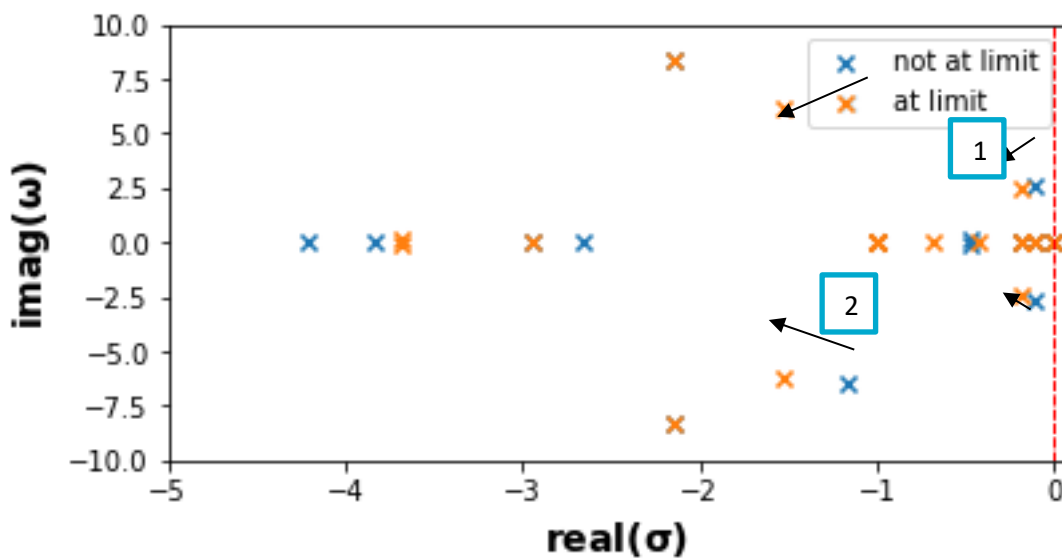


Figure 47: Zoomed in comparison of eigenvalues

Eigenvalues in region 2 are only impacted by GFL IBR and the machine in Area where the GFL IBR is situated. And both eigenvalues of regions 1 and 2 are impacted by the PLL of the GFL IBR.

Subsequently, as the PLL gains of the GFL IBR are varied and trajectory of eigenvalue is studied when IBR is not working at its current limit and when it is working at its current limit.

Figure 48 and Figure 49 shows the impact of variation of proportional gain of PLL on eigenvalues when IBR is not at its current limit and when IBR is operating at its current limit. It is observed that

proportional gain of PLL does not have a significant impact on system stability whether the IBR is operating at its current limit or not.

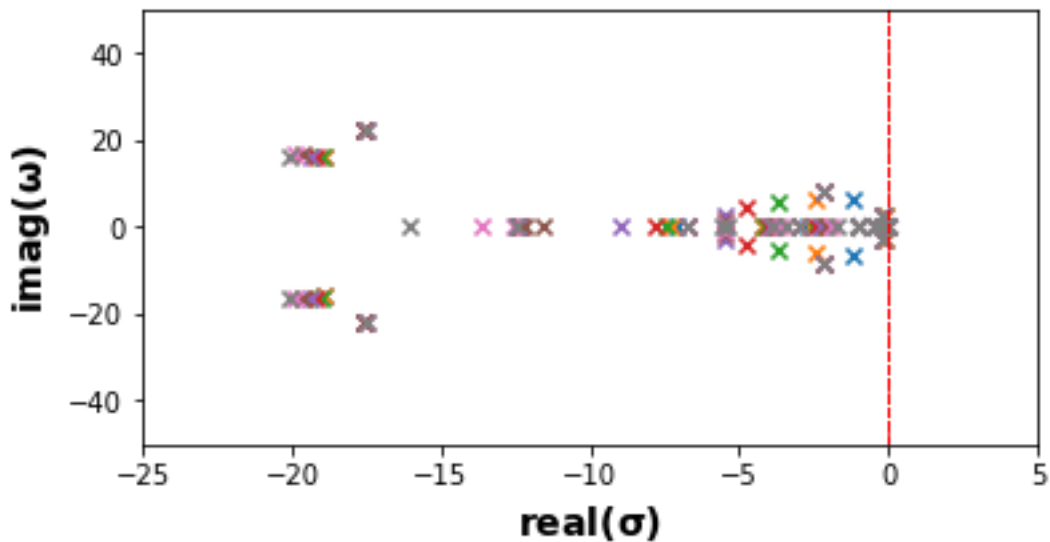


Figure 48: Eigenvalues when $k_i\text{PLL} = 50$, and $k_p\text{PLL}$ is varied from 2 to 30 (IBR not operating at its current limit)

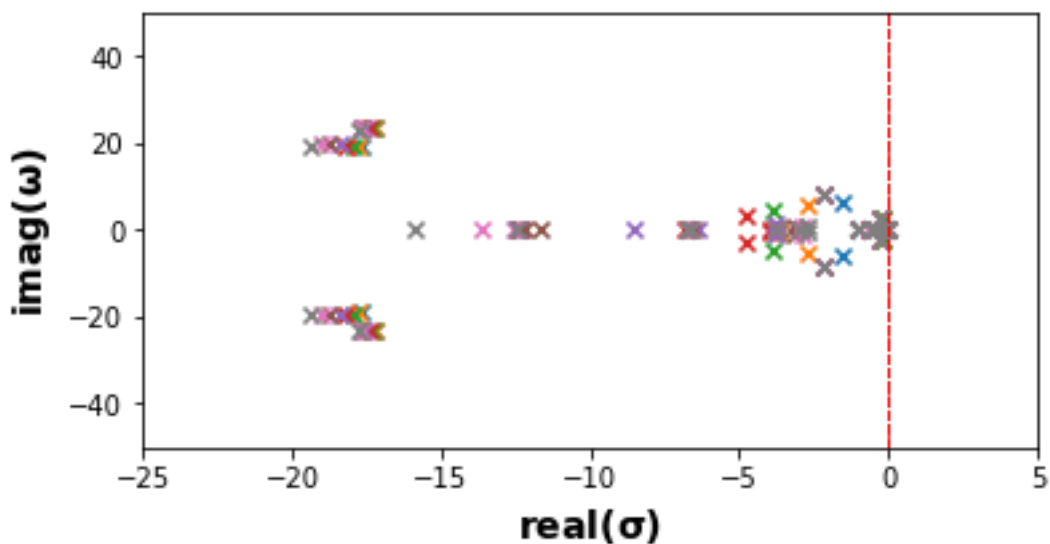


Figure 49: Eigenvalues when $k_i\text{PLL} = 50$, and $k_p\text{PLL}$ is varied from 2 to 30 (IBR operating at its current limit)

Next, the integral gain of PLL is varied from 50 to 1350, proportional gain k_p is kept at 2, results are shown in Figure 50 and Figure 51. System remains stable whether the IBR is working at its current limit or not. Eigenvalues of Region 1 are not affected by the integral gain, however eigenvalues of region 2 have different trajectories depending whether the IBR is operating at its current limit or not. For both cases it is observed that the system stability is improved when integral gain is increased up to a point, after which the eigenvalues start moving towards the imaginary axis. For both the cases (not shown here) for very high value of integral gain system becomes small signal unstable.

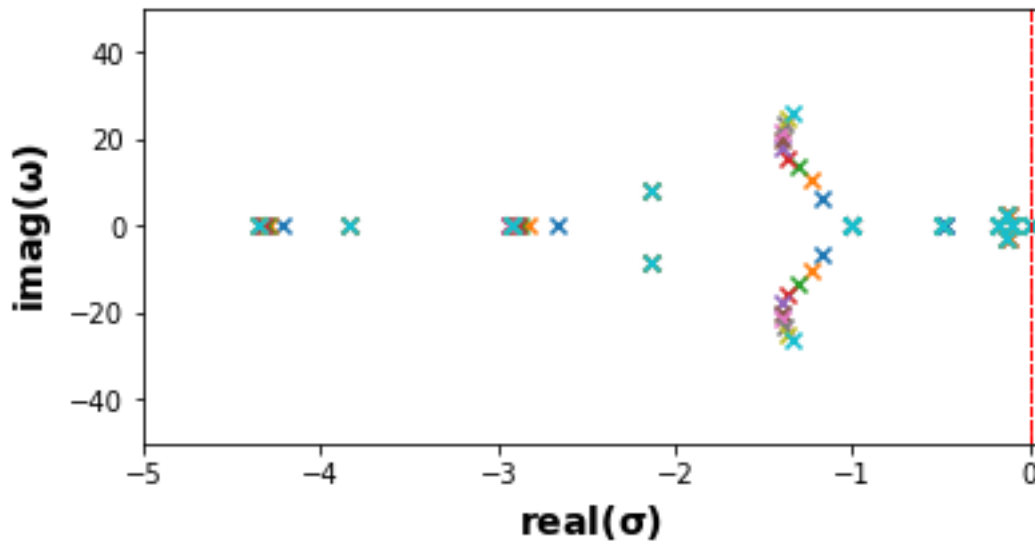


Figure 50: Eigenvalues when $k_{pPLL} = 2$, and k_{iPLL} is varied from 50 to 1350 (IBR not operating at its current limit)

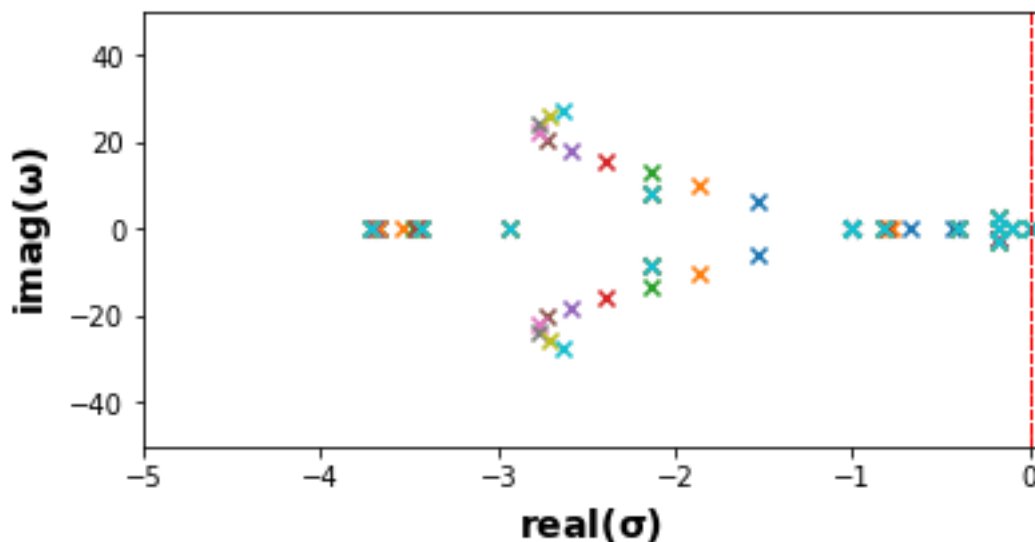


Figure 51: Eigenvalues when $k_{pPLL} = 2$, and k_{iPLL} is varied from 50 to 1350 (IBR operating at its current limit)

Case 2: Similar observations as in Case 1 is made for Case 2, and hence it is not presented here.

Case 3: In this case one GFL IBR is connected in each area, location of the IBR does not have any impact on the results. As shown in Figure 52, varying proportional gain does not have any significant impact on the system stability. However, as shown in Figure 53 higher value of integral gain leads the eigenvalues move closer to the imaginary axis in the case when the IBR is operating at its current limit.

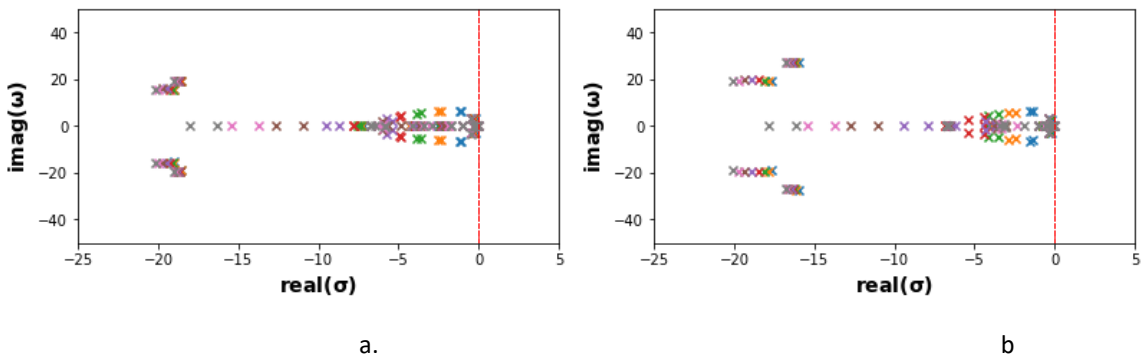


Figure 52: Eigenvalues for Case 3 varying k_p , a) not at limit b) at limit

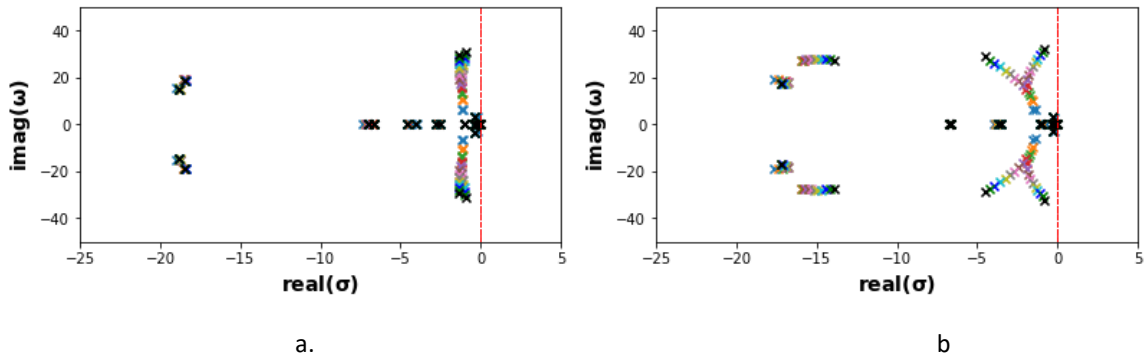


Figure 53: Eigenvalues for Case 3 varying k_i , a) not at limit b) at limit

Case 4: In this case all the SG in one area are replaced by GFL. Figure 54 shows the eigenvalue of the system when the IBRs are not operating at their limit and when they are operating at their current limit. It is observed that irrespective of the current limit being reached or not, the system becomes unstable. Dominant states associated with the eigenvalues which move to right hand side of the imaginary axis are $\Delta\omega$ and $\Delta\theta$ of SG and IBRs.

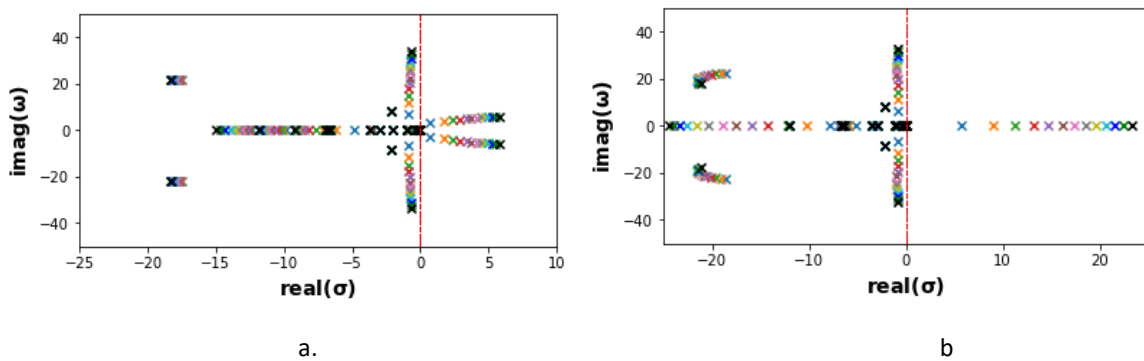


Figure 54: Eigenvalues for Case 4 varying k_i , a) not at limit b) at limit

Case 5: In this case all the SG in Area 2 are replaced by GFL IBRs. Similar observations as in Case 4 is made.

Detailed study of impact of network parameters such as line length, load change, change in network configuration etc. is yet to be carried out.

8 Conclusion and future work

The following key insights are obtained from the tasks conducted in this stage of the project:

- This study compared a data-driven prediction method and the APM algorithms for IBR admittance with OP variation and revealed the superior performance of the APM, when the training data size is limited. Validated using a black-box model, this approach demonstrates promising applicability for enhancing grid stability in power systems incorporating IBRs.
- For the small test circuits, the small signal modelling/analysis framework was validated against available test data or PSS[®]E simulations, indicating that the small signal modelling framework accurately modelled the network dynamics for those networks. Similarly, for the synthetic NEM network the small signal framework accurately indicated a presence of poorly damped or sustained/unstable oscillations for a network with a large number of IBRs, indicating that such a tool might be used in the future as a screening mechanism to identify potential unstable conditions in the network while not requiring a prohibitive amount of computational time/resources.
- It was observed that for the small two-area network, the positive sequence network representation was sufficient when the network was synchronous generator dominated, and resulted in similar eigenvalues and modes as when a detailed EMT network representation was used during the small signal analysis.
- It was observed that the network oscillatory modes were impacted by the load model selected during the dynamic simulations (as well as small signal analysis), and this highlights the importance of selecting the load model carefully when performing a small signal stability analysis or a time domain positive sequence stability analysis.
- The procedure to develop an approximate state space model representing IBRs in a small signal study based on just the frequency domain impedance characteristics (such as from a blackbox IBR model) was validated against the analytical IBR model – the validation was performed both for the model in isolation as well as when the model was incorporated in the synthetic NEM network small signal framework. The approximate models developed based on the frequency scans were able to replicate the damping provided by the detailed analytical models of the same IBRs. Successful application of this procedure indicates the usefulness of this procedure to incorporate blackbox IBR models in small signal assessment studies, including for a large network assessment.

Some avenues for future work based on this research can be:

- The admittance estimation algorithm can be further enhanced by testing it for different black box IBRs with different control configurations, for example, different control architectures representing grid following and grid forming IBRs, or IBR control configurations operating in different modes or using different additional control signals or measurements.
- In this project, the developed analysis framework was applied to synthetic networks, including smaller benchmark networks and a large synthetic network spanning the area served by NEM. A next step can be to apply the framework to an actual utility network. Key learnings here are

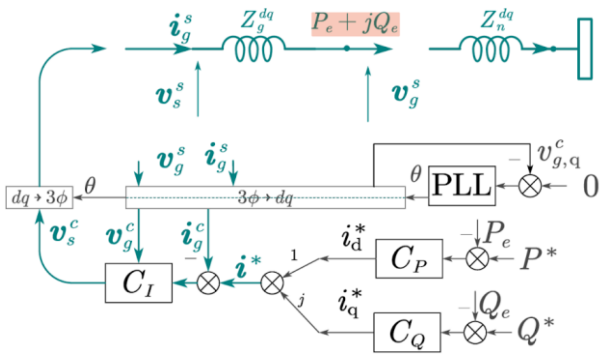
expected to be identifying practical challenges and corresponding insights that may arise when applying the framework to a real network as opposed to a synthetic network.

- EMT domain IBR models were used in this project to obtain the frequency scans, and the process of generating the frequency scans can be computationally burdensome especially if a large number of diverse IBRs are to be studied. However, there may be a possibility of using positive sequence models to identify certain aspects of the frequency domain characteristics – the applicability and limits of such approaches may be studied in a future effort.
- This stage of the project conducts a preliminary study of the impact of current limits on the small signal behaviour of IBRs. In the next stage of the project, this effort can be expanded to include the different approaches adopted in grid following and grid forming IBRs to limit the current and different responses possible (for example, giving priority to active current, reactive current, power factor) when operating at the current limit.
- A fundamental frequency network equivalent was used in this stage of the project for the large network, a comparison of using a multiple-frequency network equivalent to fundamental frequency network equivalent for a large network such as the synthetic NEM network may be made in the next stage. When using a fundamental frequency network equivalent, we may miss out on capturing some of the modes that result due to resonance conditions in the network.
- The load model was found to have a large impact on the oscillation modes observed in the simulations/analysis. A potential future work related to this insight can be to study the IBR-load interactions further by including a detailed representation of loads such as by using composite load model.
- While the procedure to incorporate IBR models in small signal studies based on impedance characteristics were demonstrated in this stage of the project, there are practical challenges that remain, such as:
 - standardization of the procedure to utilize an IBR model to obtain the frequency domain impedance characteristics.
 - understanding the of impact of measurement location that is used by control loops of the IBR,
 - defining the range of frequencies needed to be captured as well as any pre-requisite tests or requirements from the model that may be needed to apply this process for an IBR model.

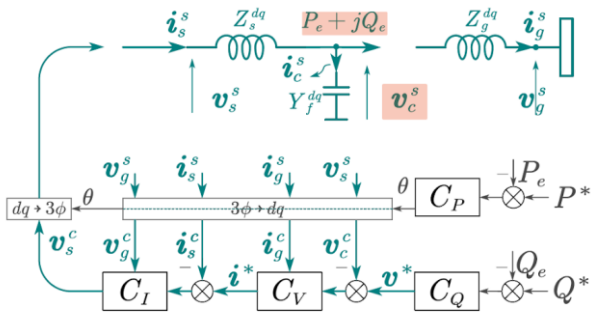
Aspects of the procedure such as the vector fitting process often need trial-and-error type input and engineering judgement, a future effort might also involve a further study of these aspects to automate the procedure as far as possible.

- Future discussions on the topic can also bring in inverter OEMs and commercial software vendors to help streamline the process of industry adoption. If inverter OEMs are involved, we can hope towards considering the inverter model as a gray box instead of a black box. With commercial software vendors involved, we can move towards having the developed stability analysis techniques adopted quicker by industry.

Appendix A Analytical models and parameters



Apx Figure A.1 Structure used for the generic GFLLI analytical model. The loop marked CQ represents either a power controlled or voltage controlled (with Q_e and Q^* replaced with V_e and V^* respectively) GFLLI.



Apx Figure A.2 Structure used for the generic GFMI analytical model. The loops marked CP and CQ represent either a VSG or PI-based power-controlled GFMI.

Apx Table A.1 GFLLI basecase parameter values

DESCRIPTION	VALUE	DESCRIPTION	VALUE
VA Power base	1e4 VA	Current proportional gain kip	3.8197 pu
AC voltage line-to-line $V_{ll,rms}$	690 V	Current integral gain kii	40 pu/s
Filter impedance L_g	0.30 pu	Current decoupling term X_f	0.30 pu
Filter ESR R_g	0.015 pu	Current loop feedforward β_i	0
Real power proportional gain kpp	0.08164823	Real power integral gain kpi	16.32964584
Reactive power proportional gain kqp	0.08164823	Reactive power integral gain kqi	16.32964584
Voltage proportional gain kvp	0.08	Voltage integral gain kvp	200

Apx Table A.2 GFMI basecase parameter values

DESCRIPTION	VALUE	DESCRIPTION	VALUE
VA Power base	1e4 VA	Voltage proportional gain kvp	0
AC voltage line-to-line $V_{ll,rms}$	690 V	Voltage integral gain kvi	200 pu / 400 pu
Filter impedance L_s	0.15 pu	Voltage decoupling term B_f	0

DESCRIPTION	VALUE	DESCRIPTION	VALUE
Filter ESR R_s	1e-3 pu	Current proportional gain k_{ip}	0.01 pu
Filter capacitance C_f	0.01 pu	Current integral gain k_{ii}	250 / 400
Paralleled resistance B_{Cf}	0.01 pu	Current decoupling term X_f	0.15 pu
Inertial constant J	2 s / 0.2 s	Q droop k_q	0.01 pu / 0.1 pu
Damping ratio D	150	Q LPF cut-off frequency ω_Q	40π
Current loop feedforward β_i	0	Voltage loop feedforward β_v	0.5
Real power proportional gain k_{pp}	0	Reactive power proportional gain k_{qp}	0
Real power integral gain k_{pi}	1.5π	Reactive power integral gain k_{qi}	1.5π

References

- [1] Electric Power Research Institute, “CSIRO Australian Research for the GPST: Topic 2 - Stability Tools and Methods,” CSIRO, 2021.
- [2] A. Rygg, “Impedance-based Methods for Small-signal Analysis of Power Electronics Dominated Systems,” 2018.
- [3] Electric Power Research Institute, “Code Based Generic Inverter Based Resource Model,” Electric Power Research Institute, Palo Alto, CA. 3002028322, 2023.
- [4] Electric Power Research Institute, “Small-Signal Stability of 100% IBR Dominated Power Systems During Blackstart: Eigenvalue Analysis and Stability Properties of Grid-Forming IBR-based Blackstart,” Electric Power Research Institute, Palo Alto, CA, 3002026981, 2023.
- [5] *Powerfactory file “nem_2300_not_SA.pfd” received from Tom Philpott, University of Wollongong, on July 13, 2022, 2022.*
- [6] Electric Power Research Institute, “Voltage Control Areas (VCA) Studio,” Electric Power Research Institute, Palo Alto, CA, 3002025866, 2022.
- [7] Electric Power Research Institute, “Grid Strength Assessment Tool,” Electric Power Research Institute, Palo Alto, CA. 3002024263, 2022.
- [8] Electric Power Research Institute, “REGC_C Implementation in PSS/E (REGC_C (PSS/E)) v1.2,” Electric Power Research Institute, Palo Alto, CA. 3002020781, 2021.
- [9] P. Kundur, *Power System Stability and Control*, McGraw Hill, 1994.
- [10] M. A. Pai, *Energy Function Analysis for Power System Stability*, Boston: Kluwer Academic Publishers, 1989.
- [11] Electric Power Research Institute, “EPRI UNIFI Consortium Work Progress: 2022 - 2023,” Electric Power Research Institute, Palo Alto, CA. 3002030336, 2023.
- [12] C. P. Robert and G. Casella, *Monte Carlo Statistical Methods*, 1 ed., vol. 2, New York, NY: Springer, 1999.
- [13] A. Rygg, M. Molinas, C. Zhang and X. Cai, “A Modified Sequence-Domain Impedance Definition and Its Equivalence to the dq-Domain Impedance Definition for the Stability Analysis of AC Power Electronic Systems,” *IEEE Journal of Emerging and Selected Topics in Power Electronics*, vol. 4, no. 4, pp. 1383 - 1396, 2016.
- [14] B. Gustavsen and A. Semlyen, “Rational approximation of frequency domain responses by Vector Fitting,” *IEEE Trans. Power Delivery*, vol. 14, no. 3, pp. 1052-1061, 1999.
- [15] B. Gustavsen, “Improving the pole relocating properties of vector fitting,” *IEEE Trans. Power Delivery*, vol. 21, no. 3, pp. 1587-1592, 2006.
- [16] D. Deschrijver, M. Mrozowski, T. Dhaene and D. De Zutter, “Macromodeling of Multiport Systems Using a Fast Implementation of the Vector Fitting Method,” *IEEE Microwave and Wireless Components Letters*, vol. 18, no. 6, pp. 383-385, 2008.

- [17] F. Arraño-Vargas and G. Konstantinou, "Synthetic Grid Modeling for Real-Time Simulations," in *2021 IEEE PES Innovative Smart Grid Technologies - Asia (ISGT Asia)*, Brisbane, Australia, 2021.
- [18] R. Heidari, M. Amos and F. Geth, "An Open Optimal Power Flow Model for the Australian National Electricity Market," in *2023 IEEE PES Innovative Smart Grid Technologies - Asia (ISGT Asia)*, Auckland, New Zealand, 2023.
- [19] T. Philpott, A. P. Agalgaonkar, K. M. Muttaqi, T. Brinsmead and H. Ergun, "Development of High Renewable Penetration Test Cases for Dynamic Network Simulations using a Synthetic Model of South-East Australia," in *2023 IEEE International Conference on Energy Technologies for Future Grids (ETFG)*, Wollongong, Australia, 2023.

As Australia's national science agency and innovation catalyst, CSIRO is solving the greatest challenges through innovative science and technology.

CSIRO. Unlocking a better future for everyone.

Contact us

1300 363 400
+61 3 9545 2176
csiro.au/contact
csiro.au

For further information (position for single contact only, delete if more and use below only)

Insert Business Unit name
Insert contact name
+61 0 0000 0000
first.last@csiro.au
csiro.au/businessunit

For further information (position for up to four contacts, delete all if single contact and use above only)

Insert Business Unit name
Insert contact name
+61 0 0000 0000
first.last@csiro.au
csiro.au/businessunit

Insert Business Unit name
Insert contact name
+61 0 0000 0000
first.last@csiro.au
csiro.au/businessunit

Insert Business Unit name
Insert contact name
+61 0 0000 0000
first.last@csiro.au
csiro.au/businessunit

Insert Business Unit name
Insert contact name
+61 0 0000 0000
first.last@csiro.au
csiro.au/businessunit